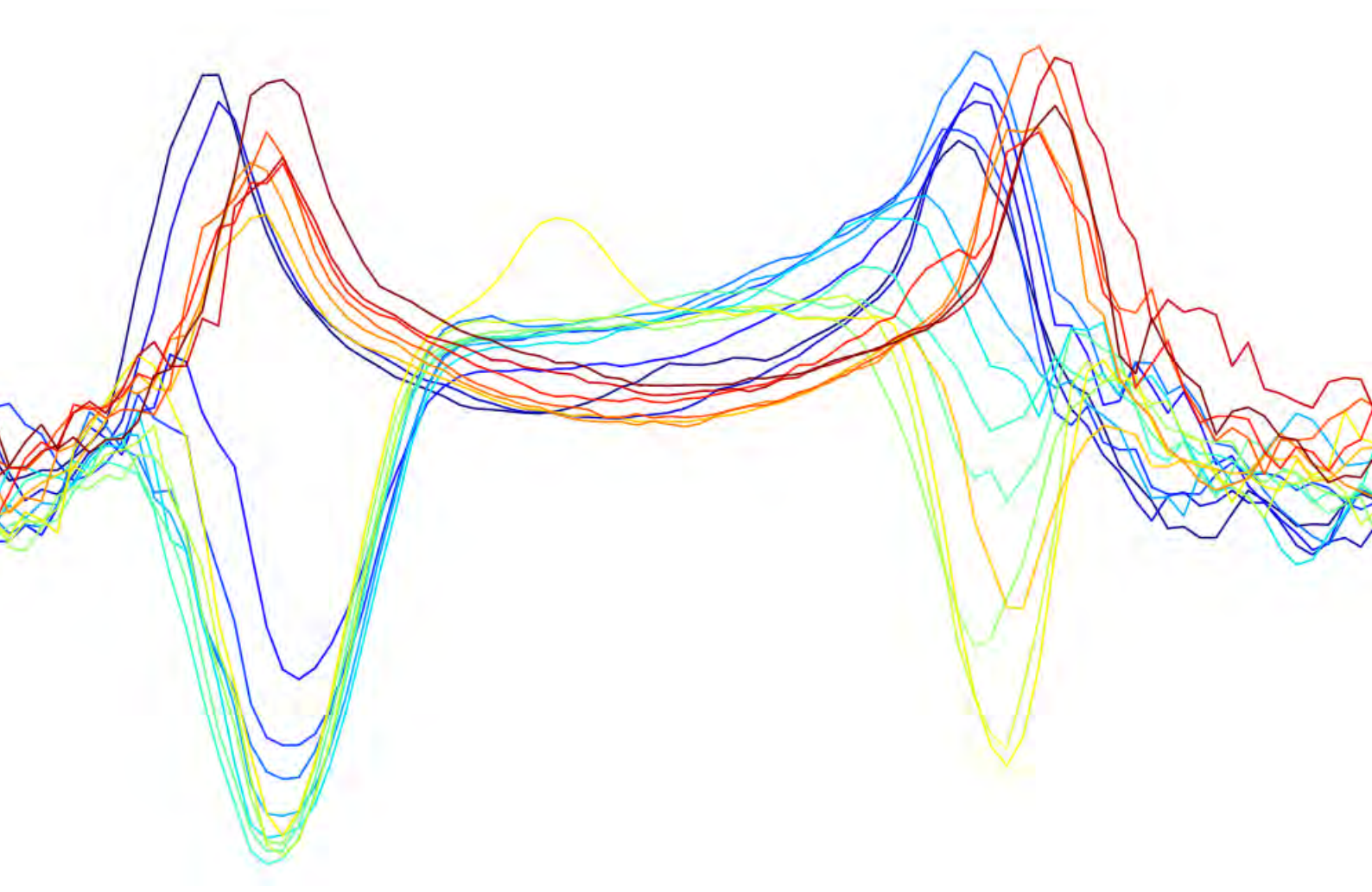


# 'LOOKING INSIDE' A PEROVSKITE

ANALYZING THE PROCESSES AT THE NICKEL OXIDE INTERFACE BY MEASURING THE  
PHOTOLUMINESCENCE OF HOLE-ONLY INTERDIGITATED BACK CONTACT PEROVSKITE  
DEVICES UNDER BIAS



Toon Maassen

Hybrid Solar Cells, AMOLF

University of Amsterdam & Vrije Universiteit

Supervised by MSc. Imme Schuringa, Prof. Dr. Bruno Ehrler & Prof. Dr. Erik Garnett

January 2022



*"Avoiding climate breakdown will require cathedral thinking. We must lay the foundation while we may not know exactly how to build the ceiling."*

- Greta Thunberg

*"Needless to say, the implications of cheap solar power would be truly staggering, revolutionizing virtually every aspect of life and geopolitics. Potentially dangerous nuclear power would become obsolete; dirty energy sources like coal and oil would be a thing of the past; and the world would no longer have to kowtow to corrupt governments that just happen to be resource-rich."*

- Max Miller



# Acknowledgments

This thesis would not have been possible without the committed and heartfelt support from the community of AMOLF. There are a few people I would like to thank in particular.

First of all, I would like to thank Imme Schuringa, for her non-wavering support, chemical knowledge, critical thinking, and joyfulness. She stood side-by-side during the most uplifting, and the most challenging moments of this research project. I thank Bruno Ehrler, for always being available for in-depth questions on the remarkable world of perovskite physics, for his fruitful guidance and support and for welcoming me back at this great place. I thank the entire nanolab staff; Bob Drent, Igor Hoogsteder, Dimitry Lamers, Hans Zeijlemaker, and Johan Derks, for their continuous support in making all the challenging fabrication processes work. Special thanks go to Dion Ursem and Hincó Schoenmaker, for always amazing me with solving any technical challenge within any timeframe. Special thanks also go to Moritz Schmidt, for sharing his intelligent thoughts on perovskite physics and helping with the modelling of a hole-only device. I would like to thank Erik Garnett, for willing to be my examiner from the University of Amsterdam. I would also like to thank Felix Deschler for taking the time to think along with the interpretation of the 'Pandora's box' of results. Of course I want to say a big thank you to the entire Hybrid Solar Cells group for all their input, support and the good time together. Last but not least, I would like to thank the entire support staff, they make AMOLF into the remarkably well functioning and welcoming research institute that it is. It has been a great adventure.



# Abstract

A major hurdle towards the optimization of perovskite solar cells are the loss mechanisms at the interface between perovskite and the transport layer. To analyze the processes at the interface we develop a novel setup, in which the spatially resolved photoluminescence (PL) is measured of nickel oxide hole-only interdigitated back contact (IBC) devices under varying voltage bias. For reference and optimization, we fabricate stacked cells, we run a drift-diffusion model, measure the system resistance, and measure the current-voltage characteristics of hole-only IBC devices. With increasing bias going from 0 to 20 V, the PL of the hole-only IBC device is scanned in lines going from one contact to the other, thereby being able to measure both above the contacts, at the edge of the contacts and in between the contacts. These measurements can distinguish various processes across the device, such as increased charge density due to the injected hole current, and increased self-absorption due to a reflective back.

Concerning the processes at the interface two main processes are discernable. First, our drift-diffusion model as well as the PL measurements indicate that the interface of nickel oxide and perovskite features significant hole accumulation with associated upward band bending. Second, the slow bias-induced decrease in photoluminescence above the edge of the contact show that ion migration plays an important role at the interface. The architecture of the IBC device combined with a voltage bias, makes it possible to disentangle and localize various processes. This research therefore shows the potential of this setup to further analyze the mechanisms at play at the interface.





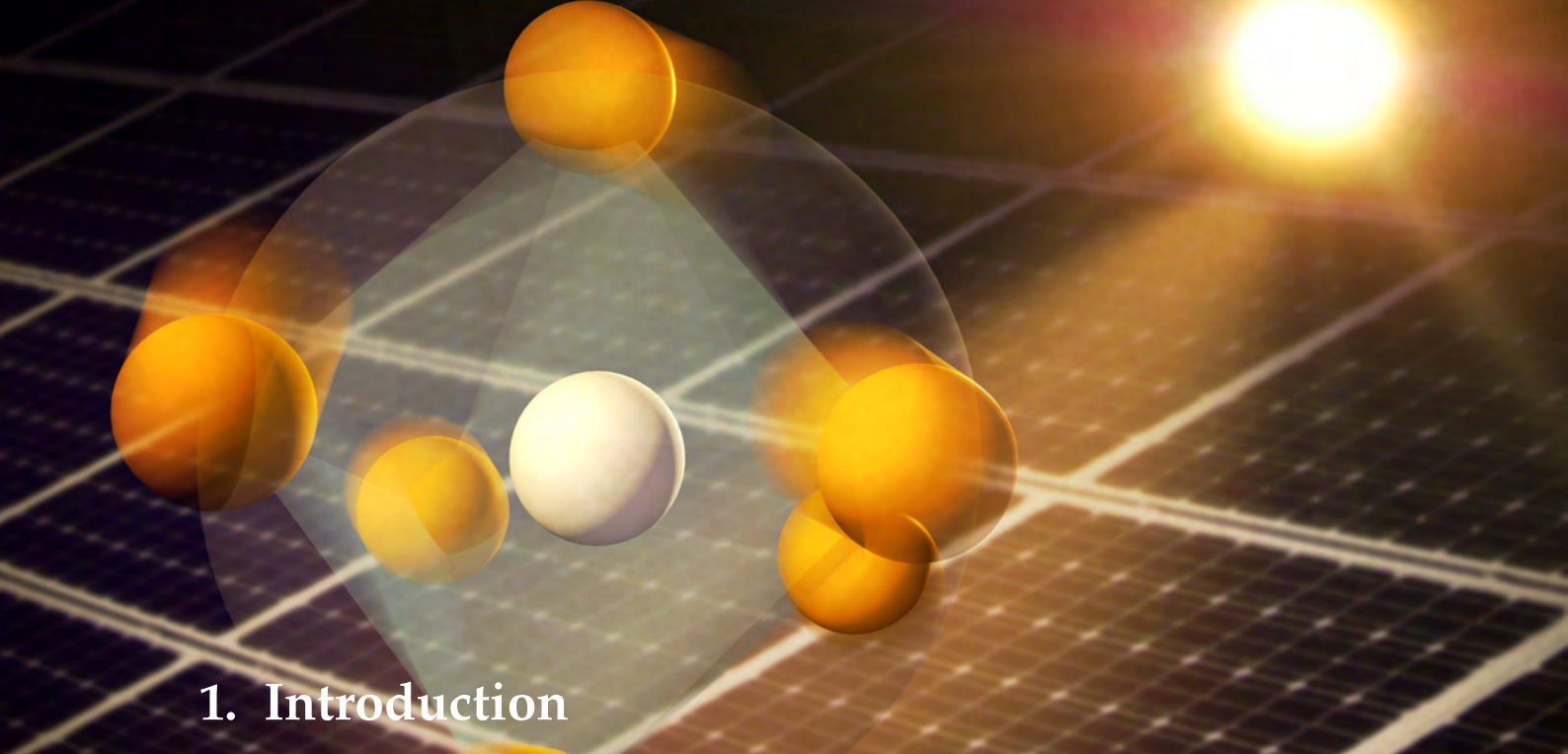
# Contents

Acknowledgments	iii
Abstract	v
Contents	vii
1. Introduction	3
2. Theoretical Background	7
2.1. Charge generation and extraction in a semiconductor	7
2.2. Current-voltage characteristics of a solar cell	8
2.3. The detailed balance limit	9
2.4. Perovskite as a solar cell semiconductor	10
2.5. Loss mechanisms at the interface	11
2.6. Hole-only interdigitated back contact devices	12
2.6.1. Interdigitated back contact devices	13
2.6.2. Hole-only devices	15
2.7. Nickel oxide as a hole transport layer	15
2.8. Measuring photoluminescence	16
2.8.1. Photoluminescence under bias	16
3. Methods	19
3.1. Fabrication of hole-only IBC devices	19
3.1.1. Cleaning quartz samples	19
3.1.2. Spincoating adhesion layer and photoresist	20
3.1.3. UV exposure and development	20
3.1.4. Evaporation of silver and nickel layer	20
3.1.5. Lift off procedure	21
3.1.6. Annealing to NiO <sub>x</sub>	21
3.1.7. Perovskite layer	22
3.1.8. Protective layer	23
3.2. Fabrication of stacked reference cells	23
3.2.1. Substrates	23
3.2.2. Cleaning of samples	24
3.2.3. NiO <sub>x</sub> layer	24
3.2.4. PTAA layer	24
3.2.5. Perovskite layer	24
3.2.6. C <sub>60</sub> + BCP layer and Ag top contacts	24
3.3. Drift-diffusion simulation	25
3.4. Measuring current-voltage characteristics	26
3.4.1. Stacked reference cells with solar simulator	26
3.4.2. Measuring the current-voltage characteristics of an IBC cell	26
3.5. Spectral PL measurements, spatially resolved under bias	27
4. Results & Discussion	31
4.1. Stacked reference cells	31
4.1.1. Optimized reference cell	31
4.1.2. Nickel oxide optimization	32

4.2. Current-voltage measurements of the IBC cells . . . . .	32
4.2.1. IBC devices . . . . .	33
4.2.2. Contacting test . . . . .	33
4.3. Drift-diffusion simulation . . . . .	34
4.4. Spectrally and spatially resolved PL measurements under bias . . . . .	35
4.4.1. PL spectra on and off contact . . . . .	35
4.4.2. Spatially resolved PL with varying bias of Ag device . . . . .	36
4.4.3. Spatially resolved PL with a varying bias of Ag + NiO <sub>x</sub> device . . . . .	38
<b>5. Conclusions &amp; Outlook</b>	<b>41</b>
<b>Bibliography</b>	<b>43</b>
<b>A. Appendix</b>	<b>47</b>
A.1. Current during the spatially resolved PL measurements. . . . .	47
A.2. Reversed bias measurement . . . . .	48
A.3. Position of fitted peaks of spectra . . . . .	49
A.4. Color scale visualization of spatially and spectrally resolved spectra . . . . .	50
A.5. C <sub>60</sub> lift off test . . . . .	51







# 1. Introduction

**Figure 1.0:** Perovskite crystal structure in front of solar array [1].

To date the anthropogenic greenhouse emissions have caused global warming of over 1 °C compared to pre-industrial levels, endangering both the health of ecosystems as well as humanity. This warming is projected to further rise by 1.5 to 5 °C by 2100, depending on uncertainties in the climate system and future emissions [2]. In the Paris climate agreement of 2015 the international community agreed to the goal of limiting warming to well below 2 °C and to pursue efforts to limit warming to 1.5 °C [3]. As science and awareness are progressing on the damages and risks of climate change, including the risk of setting off tipping elements in the earth system, limiting warming to 1.5 °C is increasingly regarded as the safest and smartest trajectory for nature and mankind.

Limiting global warming to 1.5 °C is a momentous task and necessitates swift transitions in the ways we produce energy, transport ourselves, grow food, use land and treat nature. As the major source of anthropogenic greenhouse gasses is the burning of fossil fuels, the upscaling of sustainable energy sources such as wind and solar is crucial. To make the goal of 1.5 °C attainable, the International Renewable Energy Agency projected that the global capacity of solar energy would need to reach over 14 TW by 2050, which amounts to the 18-fold of the solar energy capacity in 2020 [4]. Making this possible necessitates solar energy technologies that are increasingly affordable, efficient, and need little time and material to produce. Over the past 15 years, a novel solar cell technology has emerged that has the potential to fulfill this promise; perovskite solar cells (PSC). Within this short time, PSC's have reached a power conversion efficiency (PCE) of 25.5% [5], nearing the record PCE of the highly optimized silicon solar cells. PSC's have various benefits over silicon solar cells. First, the elements used to form the perovskite structure can be mixed in various ratios making it possible to tune the bandgap of the material [6], which is advantageous for tandem solar cell applications [7] and leads to a higher theoretical maximum PCE [8]. Second, due to the high absorption rate of the material, the absorbing layer suffices with a thickness of well below 1 μm, which is advantageous for flexibility, sustainability, affordability, and production speed. Third, perovskite can be produced using low temperatures and a roll-to-roll process similar to the printing process of newspapers, creating the potential for high production speeds [9].

However the material grapples with several challenges as well, such as its low operational stability [10], the need for toxic materials and solvents [11, 12], and remaining energy loss mechanisms. An increasingly important area of improvement is the loss mechanisms at the interface of the perovskite absorber and the transport layers, as it is thought that a large part of the remaining losses is at the interface parentitewu2021main. At this interface various loss-mechanisms can occur, such as trap assisted recombination, ion migration, insufficient charge selectivity, and insufficient band alignment. To

reduce these loss mechanisms it is important to understand and disentangle these various processes at the interface. A frequently used tool to analyze a solar cell is measuring its photoluminescence (PL), spectrally or temporally resolved [13]. Previous PL studies however have limitations. When measuring the PL of a completed stacked solar cell one cannot distinguish the influence of interfaces. When tackling this by making partial solar cells, for instance comparing the PL with and without transport layer, one can distinguish the influence of the interface, but the influence of the electric field and charge extraction is lost.

In this research, we aim to answer the following question; what processes are present at the interface between nickel oxide and perovskite? To answer this question we explore a novel setup in which the PL is measured of symmetric interdigitated back contact (IBC) devices under a bias voltage. IBC devices have alternating contacts at the back of the device, rather than a stacked architecture with all layers on top of each other. When moving the PL probe across these alternating contacts, the PL can be spatially resolved, measuring both above the contact, above to the edge of the contacts, and above the absorber material (in between the contacts). To include the influence of an external electric field, a bias voltage is added. As mixed cation/mixed halide perovskite recipes have shown the ability to produce uniquely efficient and stable solar cells [14], we use such a mixed perovskite recipe: formadinium cesium lead iodide bromide. A comparison is made between an IBC device without transport layers and a hole-only nickel oxide IBC device. Nickel oxide is chosen as a transport layer as it is compatible with the lithography of the IBC contacts and it has close band alignment with the perovskite. A hole-only device is chosen as this allows for a single IBC lithography process and isolates the effects of the nickel oxide transport layer. As a reference, stacked solar cells are produced as well and measured under a solar simulator. Figure 1.1 shows a drawing of the main setup of this research. Together these measurements can shine a new light on what happens at the nickel oxide perovskite interface.

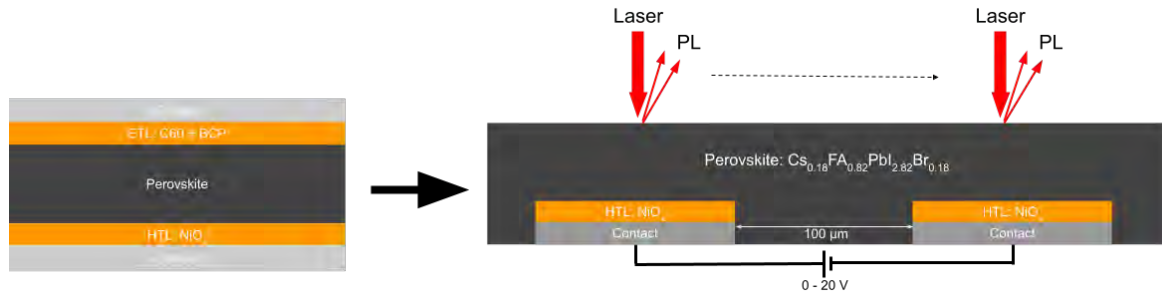
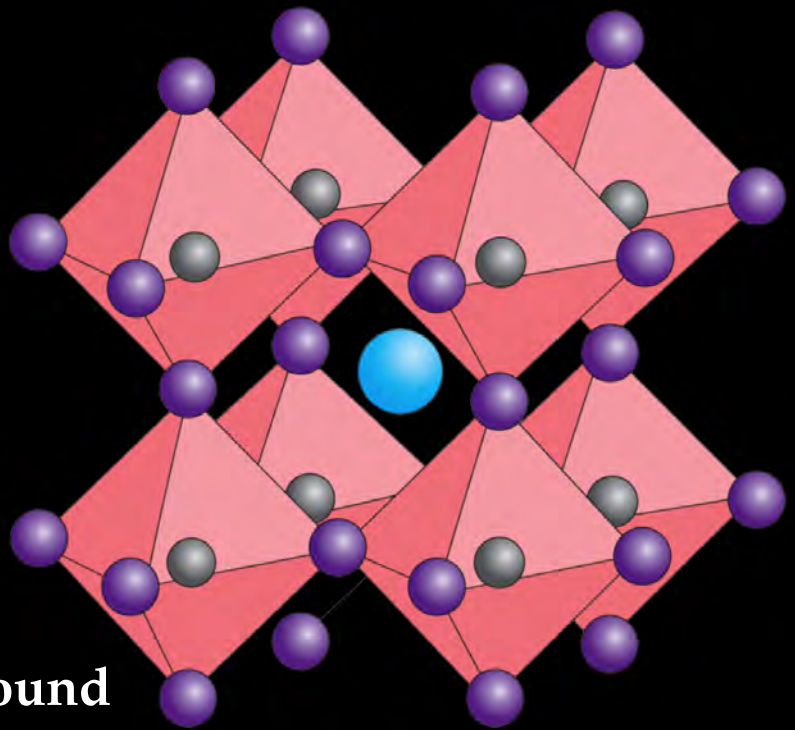


**Figure 1.1.:** Schematic drawing of main setup, measuring the PL of a biased hole-only IBC device (right) versus a stacked complete solar cell (left).









## 2. Theoretical Background

**Figure 2.0:** Perovskite crystal structure [15].

### 2.1. Charge generation and extraction in a semiconductor

A solar cell uses the photovoltaic effect to convert energy from incident light into energy. The core functional material of a solar cell is a semiconductor, characterized by its medium size bandgap between the top valence band and the bottom conduction band, as opposed to a conductor with no bandgap and an insulator with a large bandgap (see Figure 2.1). The most common semiconductor for a solar cell is silicon, other examples are cadmium telluride (CdTe), copper indium gallium diselenide (CIGS), various organic materials, and perovskites.

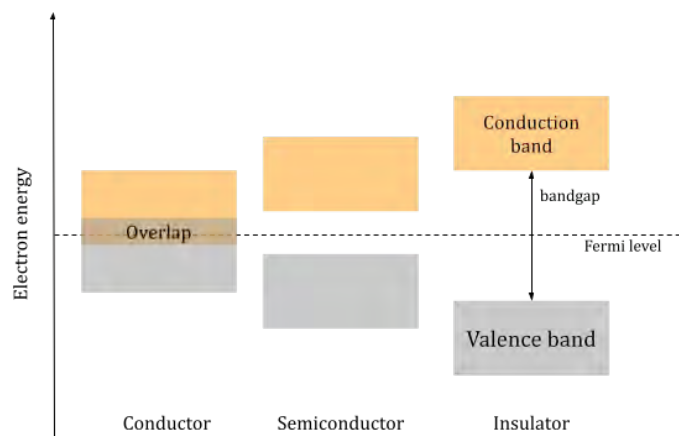


**Figure 2.1.:** Schematic drawing of bandgap structure of a conductor, semiconductor and insulator

A photon with an energy higher than the material's bandgap can excite an electron, moving it from the valence band to the conduction band, carrying enough energy to be able to move freely through the crystal. The excited electron leaves behind a gap in the crystal structure, which is referred to as an electron hole, or simply a hole. As neighboring electrons can fill this hole, thereby moving the gap, the hole can move around as well and can be described as a positively charged excited particle. The goal of a

solar cell is to harvest the energy stored in the potential difference between an excited electron and hole, by separating these charges and extracting them at opposite electrodes. This charge separation is realized by a p-n junction; a combination of a material with holes as a majority carrier (p-type) and a material with electrons as majority carrier (n-type).

In a silicon solar cell, this p-n junction is most commonly created by p-type doping one part of the silicon and n-type doping another part. In perovskite solar cells, however, separate transport layers between the perovskite and metallic contacts are added. The band structures of these transport layers are chosen in such a way that their energetic alignment blocks one type of charge and transmits the other. An electron transport layer (ETL) transmits electrons and blocks holes, whereas a hole transport layer (HTL) does the opposite. Figure 2.2 shows a schematic drawing of the photogeneration of an excited electron-hole pair that is separated and then extracted, both represented in space (a) as well as in the band structure (b). The goal of solar cell science is to build affordable and stable cells that absorb as much of the solar photons as possible, creating excited electron-hole pairs with as high as possible potential difference, of which as many as possible are extracted successfully.

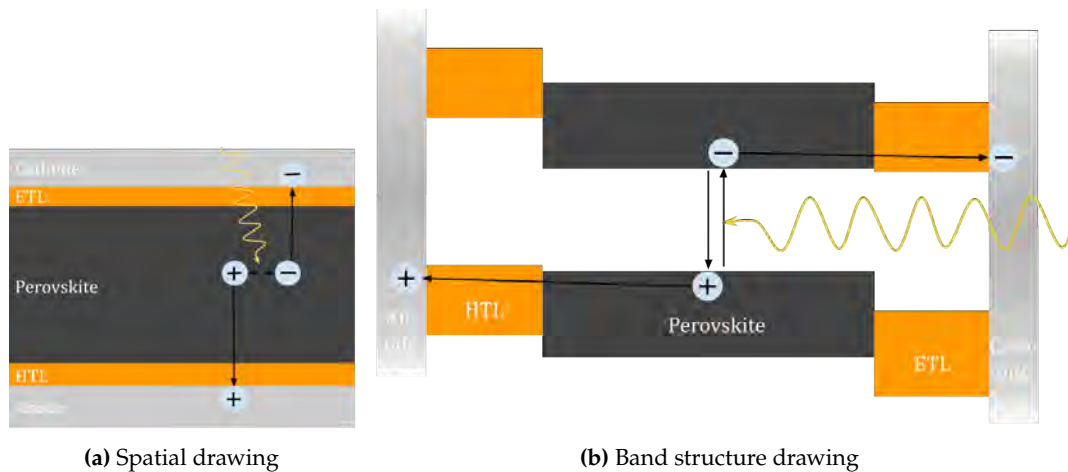
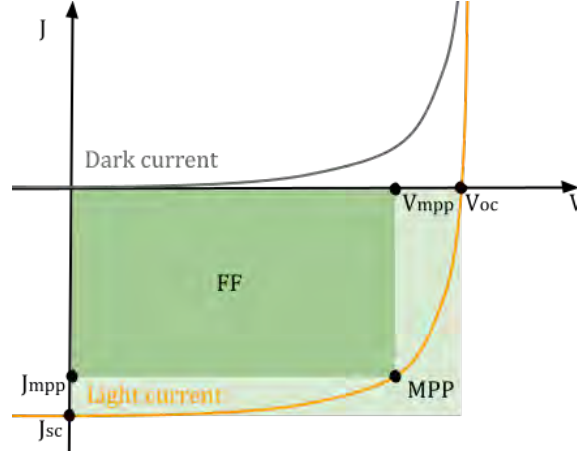


Figure 2.2.: Schematic drawings of charge generation and separation.

## 2.2. Current-voltage characteristics of a solar cell

Some of the most fundamental characteristics of a solar cell can be determined by measuring its current-voltage characteristics, or its JV curve. The current-voltage relation of a solar cell can be measured by applying a varying voltage to the cell and measuring the resultant current, both under a mimicked solar spectrum as well as in the dark.



**Figure 2.3.:** A schematic drawing of a dark and light JV curve and its most important parameters.

Figure 2.3 shows a schematic drawing of a typical dark and light current of a solar cell. Various important parameters that can be derived from such a curve are described in this section. The short circuit current ( $J_{sc}$ ) is the current flowing through an illuminated cell when no voltage is applied and is short-circuited. This parameter is important to understand what maximum current a cell can generate and whether enough charge carriers are created. The open-circuit voltage ( $V_{oc}$ ) is the voltage across an illuminated cell when no current is flowing through the device. This parameter is important to understand what maximum voltage a device can create and how much of the bandgap energy is converted into voltage. The maximum power point (MPP) is the voltage and current combination at which the device operates at maximum power, with corresponding  $J_{mpp}$  and  $V_{mpp}$ . A solar cell should be operated at this voltage to ensure it generates maximum power. The fill factor (FF) is the product of the current and voltage at MPP divided by the product of  $J_{sc}$  and  $V_{oc}$ :

$$FF = \frac{V_{mpp} \cdot J_{mpp}}{V_{oc} \cdot J_{sc}} \quad (2.1)$$

It is the ratio of the two green areas shown in figure 2.3. A good solar cell has an FF close as possible to 100%. The lower the FF the more loss mechanisms hamper the current or voltage. The power conversion efficiency is the electric power generated at MPP divided by the total incoming irradiance. It can also be calculated using  $V_{oc}$ ,  $J_{sc}$  and FF:

$$PCE = \frac{P_{max}}{I_{in}} = \frac{FF \cdot V_{oc} \cdot J_{sc}}{I_{in}} \quad (2.2)$$

In many cases, the shape of the curve can be used to determine what type of loss mechanisms are limiting the efficiency of the solar cell.

## 2.3. The detailed balance limit

In 1961 Shockley and Queisser calculated the theoretical efficiency limit of a single junction solar cell, by calculating the efficiency a cell could reach if it were only limited by radiative recombination [8]. Figure 2.4 shows this theoretical limit as a function of bandgap energy. Various solar cell materials are shown positioned at their record efficiency and bandgap [16].

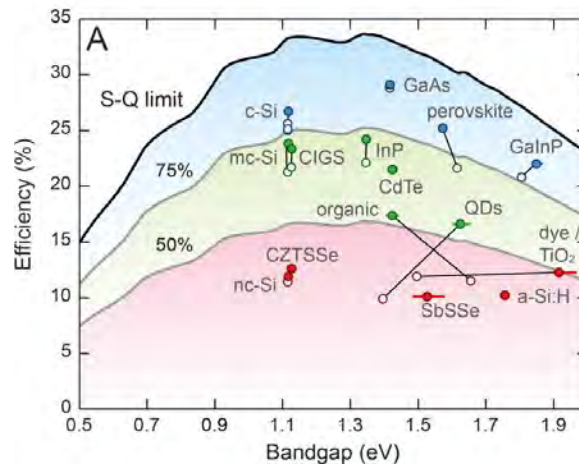


**Figure 2.4.:** 50, 75 and 100% of the detailed balance limit for AM1.5, including the record efficiencies of various solar cell materials, with open dots for April 2016 and closed green dots for July 2020 [16].

This limit takes into account the losses related to a solar cell with only one bandgap; photons with less energy than the bandgap are not absorbed and the excess energy of photons with more energy than the bandgap is lost to thermal relaxation. Therefore solar cells with multiple junctions (tandem solar cells) can beat the detailed balanced limit.

## 2.4. Perovskite as a solar cell semiconductor

Originally the term perovskite is used as the name for the mineral calcium titanate ( $\text{CaTiO}_3$ ), however, it is increasingly used to denote any material with the same octahedral crystal structure. A perovskite has the formula  $\text{ABX}_3$  where  $A$  is a cation, positioned in between the octahedrons,  $B$  is a smaller metal cation positioned in the center of the octahedrons and  $X$  is an anion positioned at the corners of the octahedrons [15]. This structure is shown in Figure 2.5. As the perovskite structure can contain uniquely large cations (in the  $A$  position) the crystal can be made up of larger organic compounds as well, leading to the possibility of organic-inorganic hybrid perovskite materials.

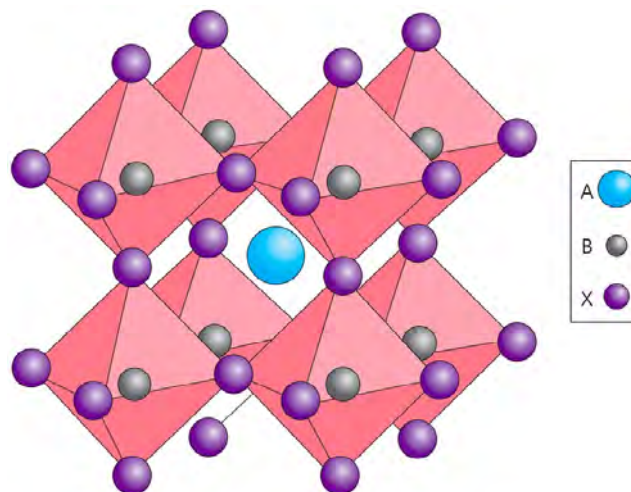


**Figure 2.5.:** The typical crystal structure of a perovskite [15].

Since the first published perovskite solar cell (PSC) in 2006 with a PCE of 2.19% (Kojima et al.) the field has shown the fastest progress in the history of photovoltaic materials, with a current single-junction

record PCE of 25.5% [5]. PSC's have various advantages. First, as different ions can be mixed in various ratios changing the optical properties of the PCE, its bandgap can be tuned to as low as 1.2 eV and as high as 3.0 eV [6]. This tunability is advantageous both to tune the bandgap close to the ideal bandgap of the detailed balanced limit, as well as for the wide bandgaps necessary in tandem solar cells. Second, perovskites feature uniquely high carrier diffusion lengths, reaching an effective diffusion length distances of more than 175  $\mu\text{m}$  [18], attributable, among others, to photon recycling [19]. Third, due to the high absorption rate of the perovskite, it can absorb most light effectively with thicknesses well below 1  $\mu\text{m}$ , as opposed to silicon with thicknesses typically above 100  $\mu\text{m}$  [20]. This means that PSC's need little material to create the active layer, which is advantageous for flexibility, production, affordability, and sustainability. Last, perovskite can be solution-processed and deposited with printing and coating techniques that are already commonly used in other fabrication processes. This enables the possibility to produce PSC's with roll-to-roll manufacturing, the same process used to print newspapers, which would dramatically increase production rates and lower prices [9].

However, PSC's currently face several challenges as well, such as limited stability, the need for toxic materials, and remaining loss mechanisms. The crystal structure of a PSC contains relatively weak bonds such as ionic bondings, hydrogen bonds, and the Van der Waals force. As a result, exposure to moisture, light soaking, heat, oxygen or electric fields can degrade the cell and lead to its limited stability. Examples of such degradation processes are the decomposition of organic compounds and the migration of ions [21, 22]. A large body of research is focussing on ways to increase the internal stability of the perovskite and its transport layers as well as efforts to improve encapsulation [10].

Another frequently mentioned challenge for perovskite is the use of lead. The most efficient perovskite solar cells use lead ions as their smaller cation (ion B in Figure 2.5), leading to concerns as lead is known for its toxicity to both human health as well as the environment. Alternatives to lead are being developed, of which the most important is tin, resulting in a significantly lower PCE; with a current record of 9.59% [23]. However, environmental analyses show that these alternatives are not necessarily less toxic [24], and that due to the uniquely thin layer of perovskites the lead pollution of a discarded PSC would be far less than toxicity soil standards and no more than the background pollution already present in industrialized countries [25].

Another major concern for the industrial-scale production of PSC's is the toxicity of the solvents used during the production of perovskite, such as dimethylformamide (DMF), dimethylacetamide (DMAC), and N-methyl-2-pyrrolidone (NMP). Therefore, methods need to be developed to produce perovskite using greener alternatives as the main solvent, such as dimethyl sulfoxide (DMSO) [26].

Last, although PSC's have seen a remarkable rise in efficiency, there still are significant loss mechanisms. Opportunities for further PCE improvement lie in the reduction of these remaining loss mechanisms. Three main areas for further improvement can be distinguished; the quality of the perovskite absorber, loss mechanisms at the interface, and effective charge separation in the transport layer [21]. As a major part of the remaining loss mechanisms relate to the interface between the transport layer and the perovskite it is becoming increasingly important to understand the loss processes at this interface and find ways to reduce them [27]. The extent to which the above-mentioned challenges can be overcome will determine the extent to which perovskite solar cells will gain commercial suitability.

## 2.5. Loss mechanisms at the interface

There are various mechanisms at and around the interface that can limit the efficiency and stability of a PSC. The most important loss mechanisms at the interface are trap-assisted recombination, insufficient band alignment, and insufficient contact selectivity. Trap-assisted recombination is a type of non-radiative recombination that is assisted by a defect or impurity in the crystal lattice. An excited electron or hole is captured in this defect, making it more likely to recombine [28]. Non-radiative recombination reduces the  $V_{oc}$  and FF. A defect is more effective at inducing non-radiative recombination when its energy level is mid-bandgap. In the bulk material of the perovskite the traps are

mostly located in or close to the valence or conduction band and are therefore not effective in facilitating non-radiative recombination, (hence the defect-tolerance of perovskite). At interface however, traps are more often energetically located within the bandgap, which makes trap-assisted recombination an important loss mechanism at the interface. Insufficient band alignment occurs when the valence band of a hole transport layer or the conduction band of an electron transport layer does not align well enough with the band of the perovskite. This misalignment hampers the transmission of the charges through the transport layer, and thereby reduces the effective charge extraction and increases recombination around the interface [29]. Insufficient contact selectivity occurs when the electron transport layer does not block holes well enough, or the hole transport layer does not block electrons well enough. When a minority carrier is not blocked and enters the transport layer, it can recombine in the transport layer or in the contact [30]. In general, when these loss mechanisms cause increased non-radiative recombination it leads to a lower  $V_{oc}$  and/or FF. A lower current density is mostly related to a decreased absorption or extraction of charge. Figure 2.6 shows a schematic band diagram with these three limiting processes around the interface.

In addition, the interface can influence the performance of the solar cell through its influence on ion migration and bulk morphology. Ion migration is a prevalent process in perovskite, as several weak bonds allow ions to migrate to other parts of the cell [31]. Ion migration is a double-edged sword, on the one hand, it can hamper the efficiency and stability of a PSC, and on the other hand, migrated ions can improve a cell through the filling of vacancies [32]. Ion migration can be influenced by the interface in three ways; first, because this migration can be facilitated by impurities at the interface; second, because it can passivate impurities and third; because effective transport layers or passivation layers at the interface can limit ion migration between the contact and the perovskite. Finally, the interface can have an influence on the bulk morphology of the crystal, as the crystal structure of the perovskite is formed on top of the bottom interface. Depending on the materials and deposition method this can both improve or worsen the performance of the cell [33].

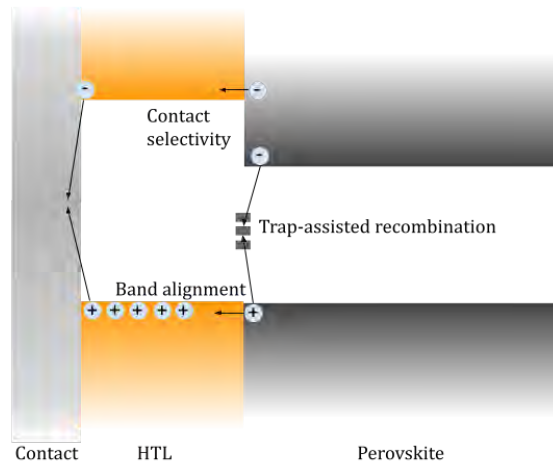


**Figure 2.6.:** Schematic drawing band diagram with various loss mechanisms around the interface.

## 2.6. Hole-only interdigitated back contact devices

In this research, hole-only IBC devices are used, with a nickel oxide transport layer at both contacts. In this section, the implications of using such interdigitated back contacts and of using a hole-only device are being discussed.



### 2.6.1. Interdigitated back contact devices

Interdigitated back contact solar cells are widely applied in the field of silicon solar cells. The record efficiency hetero-junction silicon solar cell of 26.7% is an IBC cell [34], as this avoids shading from top contacts. However, for PSC's the IBC structure is less often applied [35].

#### Electric field

In a stacked cell, the electric field is a mostly parallel field going from the cathode to the anode. However, in the case of an IBC device, the electric field has a two-dimensional distribution. In their book on electromagnetism Pollack and Stump [36] derived the electric field of a conducting strip and of an infinite conducting plane with a slot, see Figures 2.7 a and b. These electric fields resemble those of IBC contacts. One can see that the field lines at the edges of the contact are closer together, which means the electric field is stronger at the edges of the contacts compared to in the middle of the contacts.

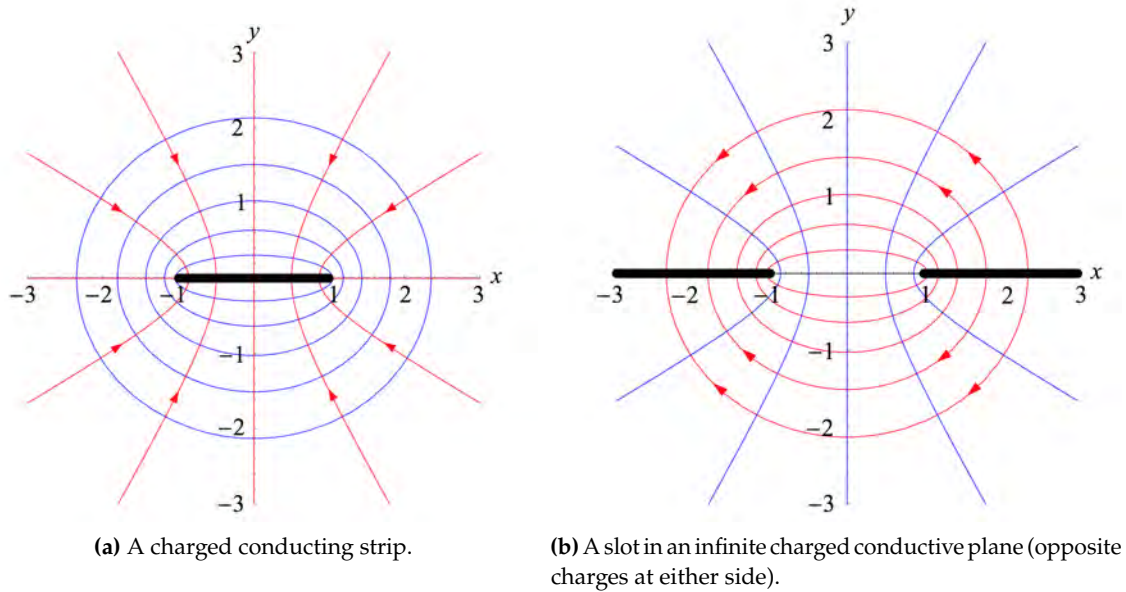


**Figure 2.7.:** Field lines (red) and equipotential curves (blue) of a charged conducting strip and a slot in an infinite plane (opposite charge at either side) [36].

They also derived the distribution of the charge density at the surface, which is described by the following equation:

$$\sigma(x) = \frac{2\epsilon_0\Phi_0}{\sqrt{a^2 - x^2}} \quad (2.3)$$

Where  $\sigma$  is the charge density,  $x$  is the position on the contact (going from  $-a$  to  $a$ ),  $\epsilon_0$  is the vacuum permittivity,  $\Phi_0$  is the potential of the strip and  $2a$  is its width. A plot of this function is shown in Figure 2.8.

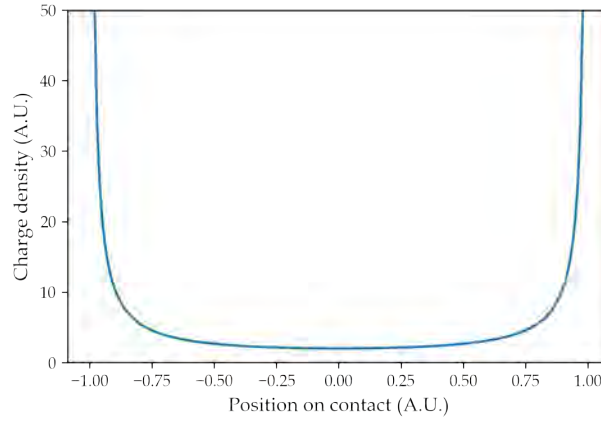


**Figure 2.8.:** Charge density distribution of a charged conducting strip (for  $\epsilon_0 = \Phi_0 = a = 1$ ).

This distribution can be understood as the exact way for the charges to create equal potential and no electric field in the x-direction across the contact, as is the case for a conductor. As both the equation as well as the plot indicate, for an infinitely thin strip, the charge density goes to infinity towards the edges of the strip. A strip with finite thickness will have very high but finite charge accumulation at the edges. This is why strong charge accumulation at the edges of the contacts is to be expected. This description assumes a vacuum around the strip. In the IBC device with a perovskite semiconductor on top of the contact, this charge accumulation at the edge will diffuse into the perovskite around the edge of the contact.

The spacing between the electrodes in our IBC cell is  $100\ \mu\text{m}$ . As the electric field is spread over  $100\ \mu\text{m}$ , rather than over  $\pm 600\ \text{nm}$  in a stacked device, a much higher voltage has to be applied to lead to the same average electric field. Assuming a homogenous distribution of the field, the voltage applied would need to be  $100/0.6 \approx 167$  times larger. It is for this reason that the IBC devices in this research are biased with larger voltages than the stacked cells. Note that, with significant charge accumulation the local electric field can become much larger than the average electric field.

## Current

The morphology of the IBC cell also means that much lower currents are to be expected than in the case of a stacked cell. Let us compare the expected ratio in current between an IBC device and a stacked device, given they have the same current density. Current density is the current divided by the cross-sectional area of the current. For a stacked cell, this area is the area of the cell itself. For an IBC device, this is the thickness of the perovskite layer multiplied by the length of the contacts, multiplied by the number of contacts minus one (the number of regions between two contacts). This is neglecting the ends of the contacts. In equation form:

$$I_{IBC} = J_{density} \cdot L \cdot T \cdot (N - 1) \quad (2.4)$$

$$I_{stacked} = J_{density} \cdot A \quad (2.5)$$

Where,  $I$  is the current,  $J_{density}$  is the current density,  $L$  is the length of the contacts,  $N$  is the number of contacts and  $A$  is the area of a stacked cell.

In our subcells the contacts have a length of  $2\ \text{mm}$ , the perovskite is  $\pm 600\ \text{nm}$  thick, and one subcell has 10 contacts with an area of  $4\ \text{mm}^2$ , see figure 2.9. This means the expected ratio between the current of a stacked cell and the current of an IBC cell for an equal current density and an equal area is:



$$\frac{I_{IBC}}{I_{stacked}} = \frac{L \cdot T \cdot (N - 1)}{A} = \frac{2 \text{ mm} \cdot 6 \cdot 10^{-4} \text{ mm} \cdot (10 - 1)}{4 \text{ mm}^2} = 2.7 \cdot 10^{-3} \quad (2.6)$$

Therefore we should take into account that the current in an IBC cell will be two to three orders of magnitudes smaller than in the reference cells.

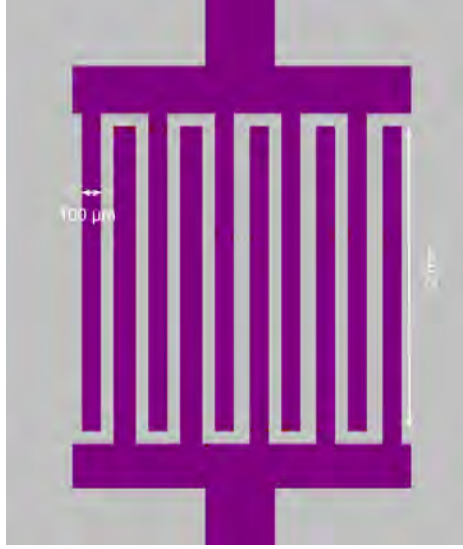


Figure 2.9.: Drawing of an IBC subcell.

### 2.6.2. Hole-only devices

As a first exploration of the applicability of biased PL measurements, this research uses symmetric hole-only devices. Making a symmetric hole-only device allows to fabricate the devices with one lithography process and isolates the effects of the nickel oxide transport layer. To be able to interpret the results of these devices it is important to understand their differences to an asymmetric device with both hole and electron transport layers. A device with only hole transport layers does not function as a p-n junction and therefore does not function as a completed solar cell.

When a bias voltage is applied to a hole-only device, a hole current flows through the device, as both hole transport layers selectively transmit holes. In terms of its JV characteristics one should not expect the typical shape of a diode, but rather resembling a linear relationship between current and voltage [37].

## 2.7. Nickel oxide as a hole transport layer

As a hole transport layer, we work with nickel oxide, for two main reasons. First, to be able to perform the lift off procedure as part of the photolithography of the IBC contacts it is best to work with a metal oxide. Second, nickel oxide is increasingly recognized as a highly efficient hole transport layer for perovskites, mainly attributable to its favorable band alignment to organic-inorganic perovskites [38], see Figure 2.10a.

Nickel oxide has a cubic crystal structure, just as sodium chloride (see Figure 2.10b). Perfectly stoichiometric (NiO) nickel oxide is an insulator. However, due to the presence of  $\text{Ni}_2\text{O}_3$  and  $\text{NiOOH}$ , in practice, oxygen is always in excess. This is the reason we denote nickel oxide as  $\text{NiO}_x$ . These nickel vacancies give the rise to free holes and make the material an intrinsic p-type semiconductor with a wide bandgap [38]. As the electronic properties of nickel oxide originate from the nickel vacancies, the properties of nickel oxide can depend on the exact deposition method. Various deposition methods for  $\text{NiO}_x$  are available such as, sol-gel processing [39], atomic layer deposition [40], spin coating of  $\text{NiO}_x$

nanoparticles [41], combustion method [42], electrodeposition [43], sputtering [44], pulsed laser deposition [45, 46], and electron beam evaporation [47]. The electron beam evaporation method is most compatible with the optical lithography process of the IBC devices, which is why we use this deposition method.

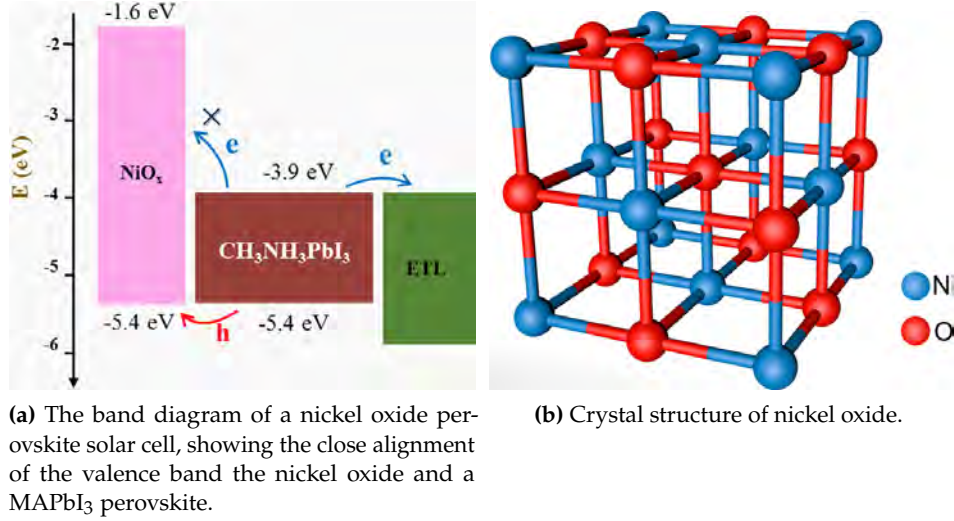


Figure 2.10.: Drawings of band alignment and crystal structure of nickel oxide [38].

## 2.8. Measuring photoluminescence

An important tool for analyzing a solar cell is measuring its photoluminescence. In this measurement, the cell is exposed to a laser, with a photon energy higher than the bandgap of the semiconductor. This will lead to the photogeneration of charge carriers. When these charge carriers later radiatively recombine, the semiconductor emits light; the PL. Analyzing this PL can give insight into which extent charges are generated, extracted, and in which ways they recombine. PL measurements can both be spectrally, spatially as well as temporally resolved [13]. When temporally resolved, the various decay processes of the photoluminescence can be distinguished. As different recombination types have different decay times, such a measurement can give insight into which processes are dominant in a cell.

### 2.8.1. Photoluminescence under bias

To gain further insights into the processes at the interface, we apply a bias voltage to the device during the PL measurements. Stolterfoht et al. carefully explained how to interpret biased PL measurements [48]. PL quenching, the reduction of PL, is often regarded as a desirable property of a solar cell, as it is assumed that this means that excited charges are effectively separated and extracted. Stolterfoht et al. explain, however, that this is not always the case, and depends on the material used and under which voltage-current condition the cell is. For a perovskite solar cell, for which exciton separation is no issue, at  $V_{oc}$ , PL quenching is undesired and means that there is significant non-radiative recombination. At  $V_{oc}$  no charges are extracted, therefore a reduction in PL is related to non-radiative recombination [48]. At a voltage under which a significant current flows through the cell, for instance, at  $V_{mpp}$ , PL quenching does indeed signify effective charge extraction. Figure 2.11 shows a clarification of these interpretations.

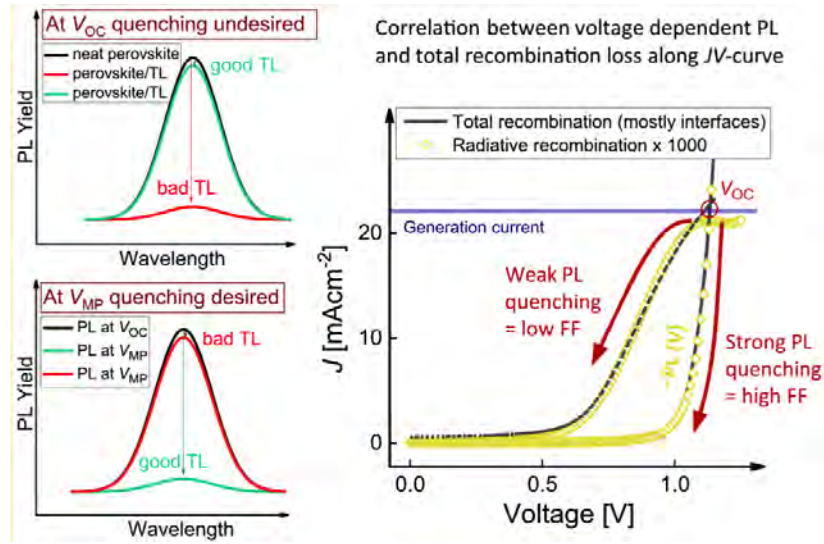


Figure 2.11.: Clarification of the interpretation of PL quenching for PSC's [48].

However, for the hole-only device, this logic does not completely apply, as excited electrons-hole pairs cannot be extracted. For a hole-only device, the quenching of PL, therefore, is a sign of non-radiative recombination, independent of the voltage applied.



## 3. Methods

**Figure 3.0:** Picture of samples being cleaned in a plasma cleaner.

In this chapter, the methods of our experiments are described. First the fabrication of hole-only IBC devices is explained, then the fabrication of stacked reference cells is explained, after that the methods of the drift-diffusion simulation are discussed, then the current-voltage measurements are explained and finally the methods of the spectrally and spatially resolved PL measurements under varying bias are explained.

### 3.1. Fabrication of hole-only IBC devices

To allow for spatially resolved PL measurements, interdigitated back contact devices are fabricated using optical lithography. A picture of the back of a finished IBC device is shown in Figure 3.1. A drawing of the IBC structure is shown in 1.1. The process of the IBC device fabrication can be summarized thusly: Using a negative photoresist, a pattern of alternating contacts is created. First, the negative resist is spin coated on top of a quartz substrate, after which the areas that should not become part of the contact are exposed to UV light, and the photoresist is developed, leaving only the parts that were exposed to UV light. Then a layer of silver and nickel is evaporated on top of the photoresist, after which it is lifted off in acetone. The devices are then annealed at 450 °C to oxidize the nickel into nickel oxide. Then a mixed halide/mixed cation perovskite and a protective layer are spin coated on top.

Here follows a more elaborate description of these fabrication steps:

#### 3.1.1. Cleaning quartz samples

15 by 15 mm fused quartz samples are used as a substrate and cleaned with the following steps. First, the samples are brushed with demineralized water and Hellmanex III soap for  $\pm 30$  seconds. Then, the

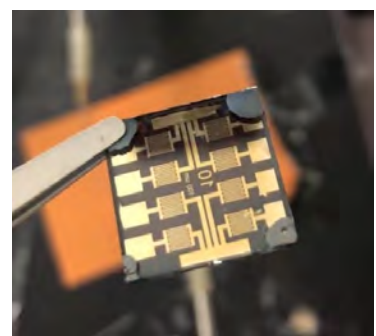


**Figure 3.1.:** The back of a finished IBC device

samples are sonicated for 12 minutes in demineralized water. After that, they are cleaned in base piranha for 10 minutes at 75°C (five parts water one part H<sub>2</sub>O<sub>2</sub> one part NH<sub>4</sub>OH). Last, they are descummed for three minutes in a Diener pico plasma-cleaner.

### 3.1.2. Spincoating adhesion layer and photoresist

First, an adhesion layer of hexamethyldisilazane (HMDS) is spin coated on the quartz in the following way. We fully cover the sample with HMDS and wait 10 seconds. Then we spin coat for 45 seconds with a speed of 4000 rpm and an acceleration of 1000 rpm/s. After which the sample is annealed for 60 seconds at 150°C.

Second, the ma-N 1420 photoresist is applied to the sample, in the following manner. We fully cover the sample with the photoresist. Then we spin coat for 30 seconds at 3000 rpm with an acceleration of 1000 rpm/s. After which the samples are annealed at 100°C for two minutes. This recipe creates a photoresist layer of  $\pm 2 \mu\text{m}$  thickness.

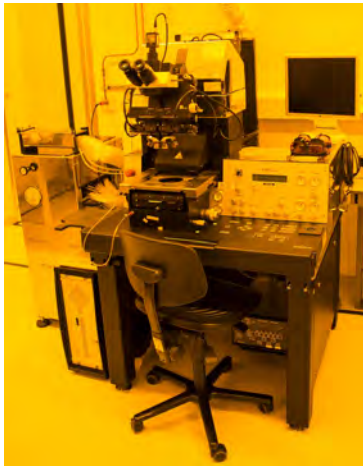


Figure 3.2.: Mask aligner

### 3.1.3. UV exposure and development

The samples with adhesion layer and photoresist are then illuminated under a patterned mask with 365 nm UV light for 22 seconds at 25 mW/cm<sup>2</sup>, to achieve a total exposure dose of 550 mJ/cm<sup>2</sup>. Figure 3.2 shows a picture of the UV mask aligner and Figure 3.3 shows a picture of the mask.

After the UV exposure, the samples are developed in the Ma-D 533/S developer, a solution based on tetramethylammonium hydroxide. The development time is  $\pm 80$  seconds. For each sample, it is checked under the microscope whether the development was complete or needs more time. An important feature of a correct development is the existence of an 'undercut'; a reclining edge at the boundary of the photoresist that allows the solvent to reach underneath the evaporated layers. If the undercut is not visible yet, the sample is developed longer in steps of 10 seconds. Figure 3.4a shows a drawing of an undercut, Figure 3.4b shows a microscopic image of a visible undercut and Figure 3.4c shows a microscopic picture of the IBC structure.

### 3.1.4. Evaporation of silver and nickel layer

After UV exposure and development, the silver and nickel layers are evaporated on top of the photoresist, using Electron Beam Physical Vapor Deposition (EBPVD). In this technique the source material is hit with a beam of electrons in a high vacuum, leading to the evaporation of the top atoms, which then precipitate as a nanolayer on the sample in the chamber. The pressure of the vacuum chamber is no more than  $2 \cdot 10^{-7}$  mbar. First, a layer of titanium is evaporated as an adhesion layer between the silver and the quartz, then the silver, and finally the nickel layer is evaporated. Table 3.1 shows the thicknesses, rates and typical e-beam current of all three layers.



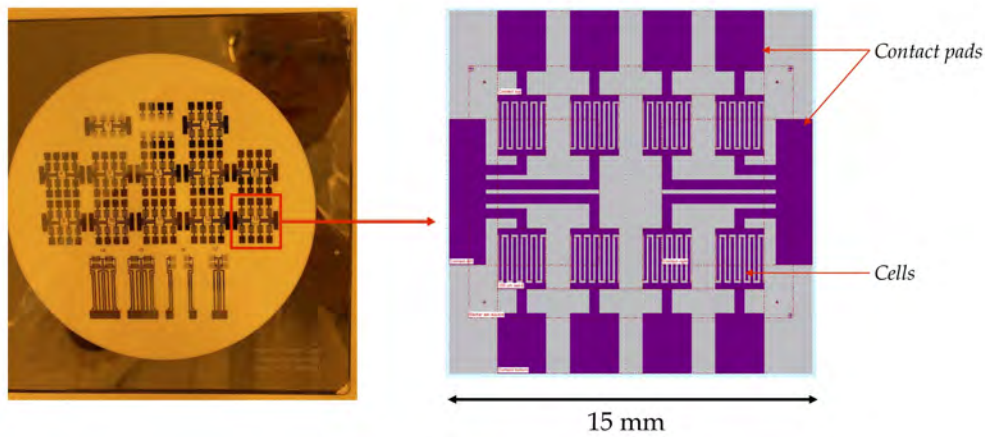


Figure 3.3.: Mask for UV spectroscopy

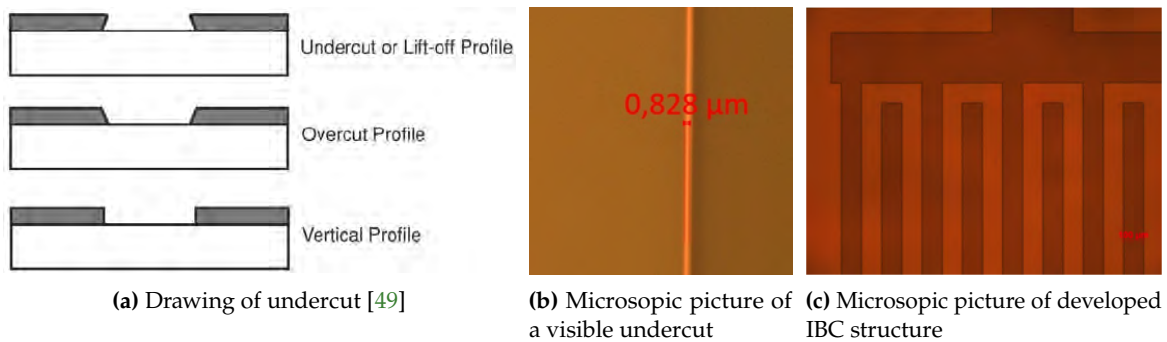


Figure 3.4.: Developing the photoresist with an undercut.

Material	Thickness	rate	emission current
Ti	3 nm	0.04 nm/s	45 ±10 mA
Ag	100 nm	0.1 nm/s	20 ± 5 mA
Ni	7 nm	0.05 nm/s	40 ±15 mA

Table 3.1.: Contact layer thicknesses and evaporation rates

### 3.1.5. Lift off procedure

After the evaporation of the silver and nickel contact layers, the samples are immersed in acetone at 50 °C to perform the lift off. The photoresist that was not dissolved in the developer now does dissolve, thereby lifting off parts of the silver and nickel layers to create the IBC pattern. The duration of the lift-off is 10 minutes to several hours, depending on how fast the metal layers are released.

We have experimented with evaporating nickel oxide reactively, in other words evaporating nickel while adding a stream of oxygen into the vacuum chamber to create nickel oxide. This was possible but leads to unstable evaporation and the layer impeded a neat lift-off. This is why we evaporate nickel and then anneal it to nickel oxide.

### 3.1.6. Annealing to $\text{NiO}_x$

After the lift-off procedure, the samples are annealed at a hot plate to oxidize the nickel to nickel oxide. The samples are heated to 450°C for 20

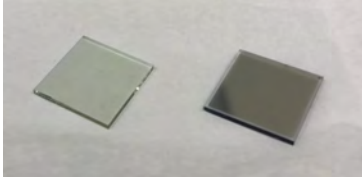


**Figure 3.5.:** Left, a sample with an annealed nickel oxide nanolayer and right, with a nickel layer before annealing.

minutes (with a 20 minute ramping up time and 60 minutes cooling downtime). Figure 3.5 shows a picture of a nickel layer and an annealed nickel oxide layer.

To verify whether the nickel oxide is completely annealed after 20 minutes of annealing at 450 °C, we have compared its absorbance after 20 and after 60 minutes of annealing. Figure 3.6 shows the result of this comparison. As the absorbance of the nickel oxide does not significantly change after 20 minutes of annealing, we conclude that 20 minutes is ample time.

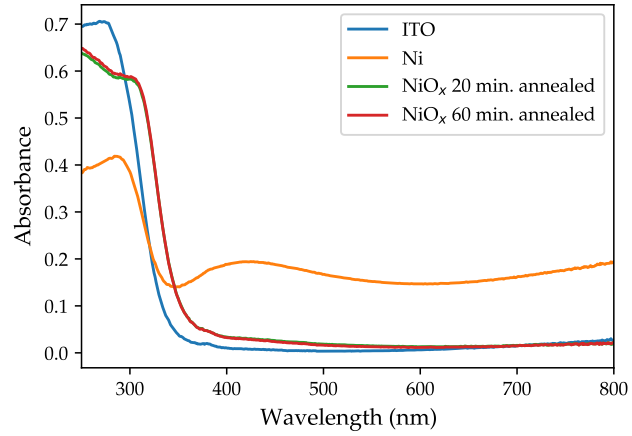


**Figure 3.6.:** Absorbance of NiO<sub>x</sub> with 20 and 60 minutes of annealing, also showing the absorbance of ITO and Ni.

### 3.1.7. Perovskite layer

Cesium bromide (CsBr), formamidinium iodide (FAI), and lead iodide (PbI<sub>2</sub>) are precisely weighed and then dissolved in dimethylformamide (DMF) and n-methyl-2-pyrrolidone (NMP). The dissolving is executed in two steps; first, the DMF is added and shaken for 5 minutes, then the NMP is added. The weights and volumes for the solution are denoted in Table 3.2. For DMF and NMP two volumes are denoted as we have experimented with a lower and a higher concentration of perovskite solution.

**Table 3.2.:** Perovskite solution ingredients.

Chemical	Amount	Supplier
PbI <sub>2</sub>	0.614 mg	TCI
FAI	0.189 mg	Greatcell
CsBr	0.0516 mg	TCI
DMF	0.9 or 1.26 ml	Sigma Aldrich
NMP	0.1 or 0.14 ml	Sigma Aldrich



**Figure 3.7.:** Picture of an IBC sample on the spin coating chuck, with perovskite solution on top.

The solution is then stirred overnight using a stirring bar at 300 rpm at room temperature ( $\pm 25^\circ\text{C}$ ). Shortly before the spin coating the solution is stirred at 100°C for 15 minutes and cooled down for 30 minutes.

65  $\mu\text{L}$  of the precursor solution is deposited on the substrate after which it is spin coated in two steps. First, it is spin coated at 2000 rpm for 10 seconds with an acceleration of 200 rpm/s. Second, it is spin coated at 5000 rpm for 30 seconds with an acceleration of 2000 rpm/s.



After 15 seconds from the start of the spin coating, the sample is quenched using a nitrogen gun for 15 seconds with a pressure of 5 bars and at 4 to 8 cm distance of the sample. Afterward, the sample is annealed at 100°C for 10 minutes.

Figure 3.8 shows the absorbance spectrum and x-ray diffraction of the perovskite used.

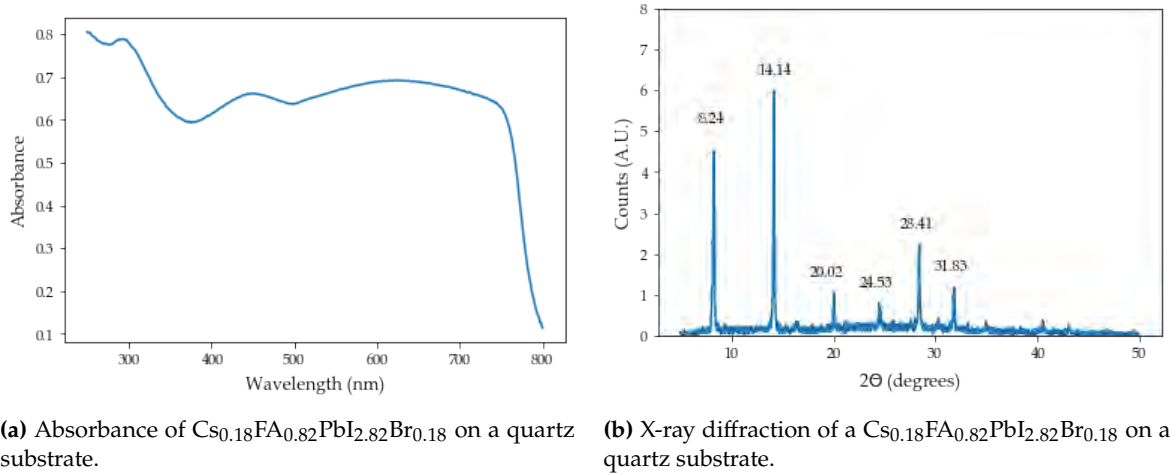


**Figure 3.8.:** Absorbance and x-ray diffraction patterns of the used perovskite.

### 3.1.8. Protective layer

As a protective coating, a layer of polymethyl methacrylate (PMMA) is spin coated on top of the perovskite layer. The 950 PMMA A8 solution from Micro Resist Technology is spin coated at 3000 rpm for 45 seconds, after which it is annealed at 95 °C for 5 minutes.

## 3.2. Fabrication of stacked reference cells

To verify and optimize the nickel oxide and perovskite layers, reference cells are produced with a non-IBC, stacked architecture. The layers that make up these cells are depicted in Figure 3.9.

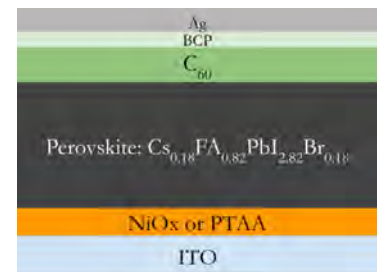


**Figure 3.9.:** Layers of the stacked reference cell.

### 3.2.1. Substrates

The substrates used for the stacked devices are 15 by 15 quartz samples with an indium tin oxide (ITO) contacting layer. The ITO layer is patterned to allow for contacting the samples correctly. Figure 3.10 shows a picture of the ITO substrate.



### 3.2.2. Cleaning of samples

The following steps are taken to clean the ITO substrates. First the substrates are brushed with demineralized water and Hellmanex III soap for  $\pm 30$  seconds. They are then sonicated three times for 12 minutes, first in demineralized water, then in acetone, and then in isopropyl alcohol (IPA). Last, they are plasma-cleaned in a Diener Zepto plasma-cleaner for 15 minutes with an oxygen pressure of 0.2 to 0.5 mbar.

Next, the hole transport layer is deposited on the cleaned samples. Two types of HTLs are used; Poly[bis(4-phenyl)(2,4,6-trimethylphenyl)amine] (PTAA) and nickel oxide ( $\text{NiO}_x$ ).

### 3.2.3. $\text{NiO}_x$ layer

To produce the  $\text{NiO}_x$  layer, the same evaporation and annealing procedure is used for the IBC cells described in section 3.1.6. The 7 nm nickel is evaporated using electron beam physical vapor deposition and then annealed at 450 °C.

### 3.2.4. PTAA layer

As a comparison to the  $\text{NiO}_x$  layer, some cells are made with a PTAA layer as an HTL. PTAA (SigmaAldrich) is dissolved in toluene (2mg/ml). Inside a glovebox (with circulation off and purging on) the sample is spin coated at 5000 rpm (with an acceleration of 5000 rpm/s) for 35 seconds. The PTAA solution is deposited on the spinning sample within the first 5 seconds of spinning, the sample is then annealed at 100°C for 10 minutes.

### 3.2.5. Perovskite layer

The perovskite layer is fabricated in the same way as with the IBC devices described in subsection 3.1.7.

### 3.2.6. $\text{C}_{60}$ + BCP layer and Ag top contacts

The electron transport layer consists of a buckminsterfullerene ( $\text{C}_{60}$ ) and bathocuproine (BCP) layer. On top of these layers, silver contacts are evaporated with a mask to create a contact pattern. All three top layers are evaporated in a thermal glovebox evaporator from the supplier Ångström. Figure 3.11 shows a picture of a finished stacked cell with the patterned top contacts. Table 3.3 shows the thickness, rates, and rotational settings of the thermal evaporations.

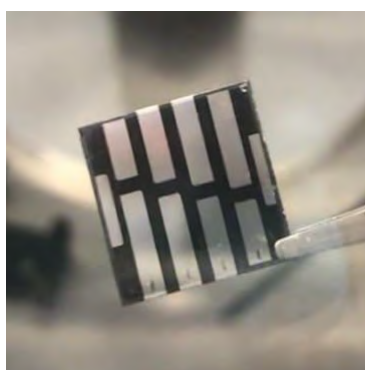


**Figure 3.11.:** Picture of a finished reference cell.

**Table 3.3.:** ETL evaporation layers.

Material	Thickness	Rate	Rotation
$\text{C}_{60}$	30 nm	0.02 nm/s	50%
BCP	8 nm	0.02 nm/s	50%
Ag	100 nm	0.1 nm/s (first 10 nm) 1.0 nm/s (afterwards)	0%

### 3.3. Drift-diffusion simulation

As a reference for the interpretation of our data, we run a drift-diffusion model, to examine the expected band diagram and charge densities in a biased hole-only device. For this simulation, we use the Setfos 5.2 semiconducting thin-film optics simulation software. As this software is not able to model 2D structures, we have simplified the IBC structure to a stacked device with a very thick perovskite layer. To limit the simulating time we have chosen a perovskite thickness of 20  $\mu\text{m}$  rather than the 100  $\mu\text{m}$  distance that is between the contacts of our real devices. As this model does not simulate the exact IBC cell, the interpretation of its results needs to be carefully executed.

Figure 3.8b shows a diagram of the energy levels of the layers including their thicknesses. Table 3.4 shows the device parameters that are used as input for this model.

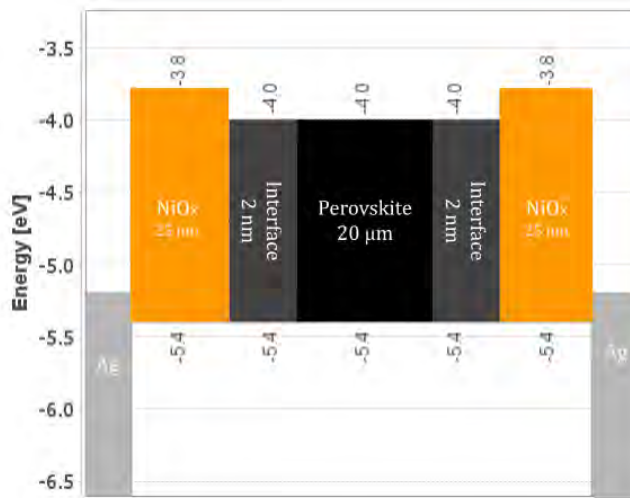


**Figure 3.12.:** Energy diagram of simulated layers.

	Ag	NiO <sub>x</sub>	Interface	Perovskite
HOMO (eV)		5.4	5.4	5.4
LUMO (eV)		3.8	4	4
N <sub>0</sub> (cm <sup>-3</sup> )		1.00e+21	1.00e+19	
Wf (eV)	5.2			
Thickness (nm)	100	25	2	2e+4
Acceptor doping		0	0	0
Donor doping		0	0	0
Dielectric constant		12	15	15
Trap density (cm <sup>-3</sup> )			1.30e+11	1.00e+11
Trap depth (eV)			0.7	0.7
Electron capture rate (cm <sup>3</sup> /s)			2.00e+11	1.00E+11
Hole capture rate (cm <sup>3</sup> /s)			2.00e+11	1.00E+11

**Table 3.4.:** Device parameters used as input for the drift-diffusion model.

### 3.4. Measuring current-voltage characteristics

#### 3.4.1. Stacked reference cells with solar simulator

The stacked reference cells are measured for their IV characteristics under light and dark circumstances. The silver contact patterns allow for eight subcells to be measured with varying areas (1.35, 2.75, 4.15, and 5.55 mm<sup>2</sup>). The cells are contacted using a sample holder, which is purposed to keep the cell isolated from the ambient air and to mask the area of the perovskite except for the subcells (see Figure 3.13a). The current is measured for a varying voltage going from -0.3 to 1.2 V for all eight subcells consecutively, in dark and under light circumstances.

The light source used is an Oriel Sol2A solar simulator, which is designed to approximate the solar spectrum with an irradiance of 1 S.

The sample holder is connected to a switching board that can measure the eight subcells one by one. The voltage and current characteristics are measured by a Keithley 2440 source meter connected to a PC.

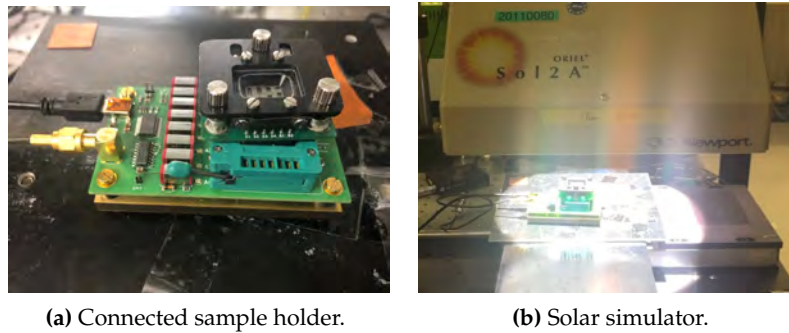


Figure 3.13.: Solar simulator setup for measuring



Figure 3.14.: Contacting an IBC device.

#### 3.4.2. Measuring the current-voltage characteristics of an IBC cell

As preparation for adding a voltage during the PL measurements, the IV characteristics of the hole-only IBC devices are explored. The devices are contacted using electric probes (see Figure 3.14). To measure the lower currents that are characteristic for the IBC devices we use the more precise Agilent B2902A precision source-measure unit, which can measure current as low as  $10^{-11}$  A and apply a voltage as high as 200 V.



Figure 3.15.: Contacting test with fully covered layers.

To verify whether the IBC cells with perovskite on top of the contacts can be contacted well using simple electric probes, we also measure the IV characteristics of unpatterned fully covered layers of Ag, Ag + NiO<sub>x</sub> and Ag + NiO<sub>x</sub> + perovskite. The IV curves of these layers are measured by simply contacting the sample at each corner, see figure 3.15. By comparing the resistance of the layers, it can be verified whether the probes pinch well through the perovskite layer and to which extent the nickel oxide layer adds resistance.

### 3.5. Spectral PL measurements, spatially resolved under bias

To measure the PL of the IBC devices both spectrally and spatially resolved, the devices are measured in a WITec microscope. With the use of a beam splitter, this microscope has the functionalities to couple a 405 nm laser into the microscope and excite the sample, while also measuring the spectrum of the PL of the sample (filtering out the reflected laser light). The sample can then be moved in the x and y direction to be able to map the PL across the contacts.

To add a voltage bias to the device during these measurements, the stage is adjusted with an extended metal plate to allow the electric probes to move along with the sample. Figure 3.16 shows pictures of this setup.

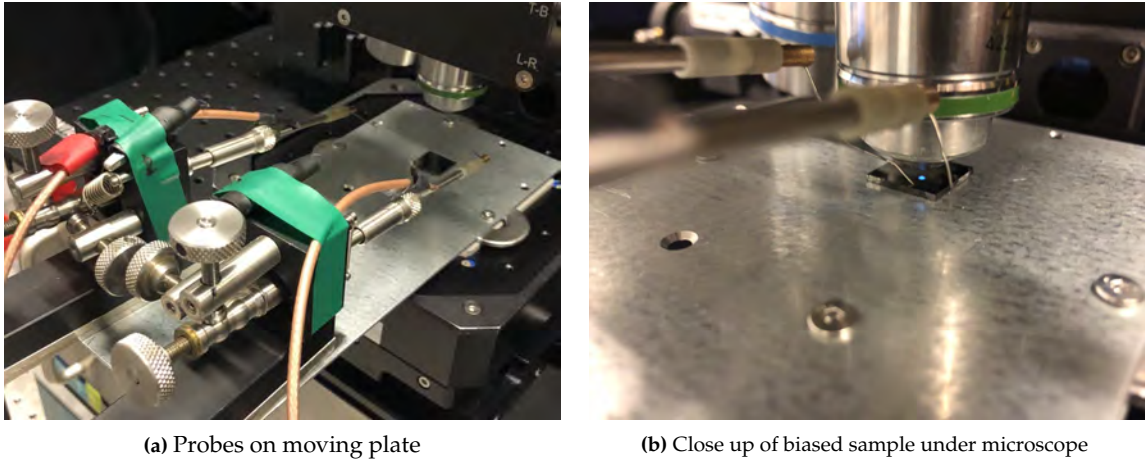


**Figure 3.16.:** Pictures of a sample being measured in the WITec microscope with probes moving along.

Line scans are made from one contact, across the perovskite to a second contact of the IBC structure. The line scans are repeated for varying voltage, each moving several  $\mu\text{m}$ 's down to avoid degradation due to the laser. Figure 3.17 shows a microscopic image of an IBC device including the lines that are scanned across the contacts. The light source is a 405 nm laser set at a power of 0.21 mW. 88 points are measured, from one contact to the next contact across 174  $\mu\text{m}$ . This means the distance between each point is 2  $\mu\text{m}$ . At each point, the PL is measured for an integration time of 150 ms. Each line scan is executed twice at a distance of 0.2  $\mu\text{m}$  from each other. Due to slightly different settings, the time in between the first and second linescan of the Ag device is 19.1 s and the of the Ag +  $\text{NiO}_x$  device is 36.4 s. For each set of two line scans the voltage is varied from 0 to 20 V in steps of 2 V. Before and after the biased measurements line scans are executed without adding any bias (an open circuit measurement).



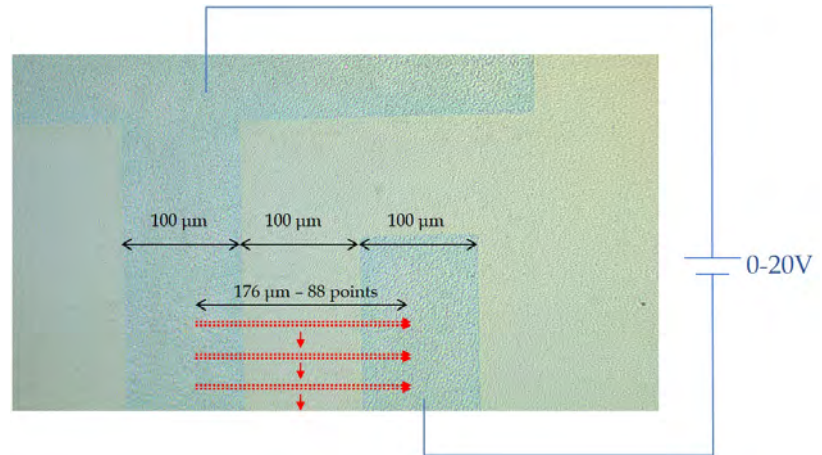


**Figure 3.17.:** Microscopic image of IBC device with a schematic drawing of the line scan (red) and bias voltage (blue). Dimensions shown in black.









## 4. Results & Discussion

**Figure 4.0:** Spatially resolved PL lines for various biases for the Ag + NiO<sub>x</sub> device, from Figure 4.9b.

In this chapter, the results of our measurements are shown and the main observations from these results are discussed. First, we discuss the results of the reference cells. Then the current-voltage measurements of the IBC cells and the results of the drift-diffusion model are discussed. We then continue with our main results regarding the spatially resolved PL of the IBC devices.

### 4.1. Stacked reference cells

To be able to optimize the materials and to verify whether the perovskite recipe and nickel oxide are functioning properly we fabricate stacked reference cells, both with PTAA and NiO<sub>x</sub> as an HTL.

#### 4.1.1. Optimized reference cell

After several rounds of optimization, the PTAA cell reached an efficiency of 13.27% and the NiO<sub>x</sub> cells reached an efficiency of 9.76%. Figure 4.1 shows the light and dark JV curves of these cells.

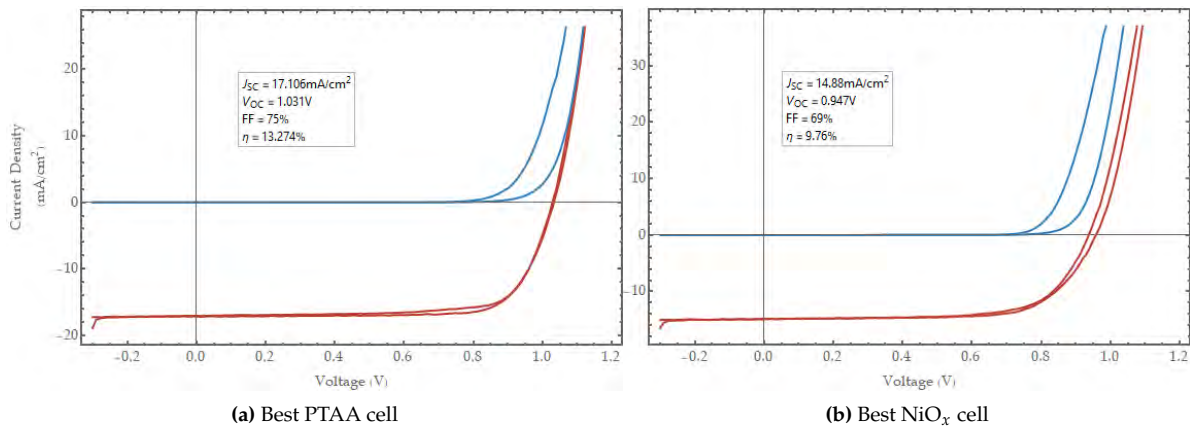


**Figure 4.1.:** JV curves for best PTAA and NiO<sub>x</sub> cell

Two important observations can be made from these JV-curves. First, the perovskite recipe does effectively work as a solar cell material, though the cells can be further optimized. Second, our evaporated  $\text{NiO}_x$  layer effectively works as an HTL though not as optimal as the PTAA layer.

#### 4.1.2. Nickel oxide optimization

Figures 4.2 a-d show the first optimization round that was performed to optimize for the thickness of the evaporated nickel before annealing. The efficiencies and currents show a thickness of 7 nm, in this case, is most optimal.

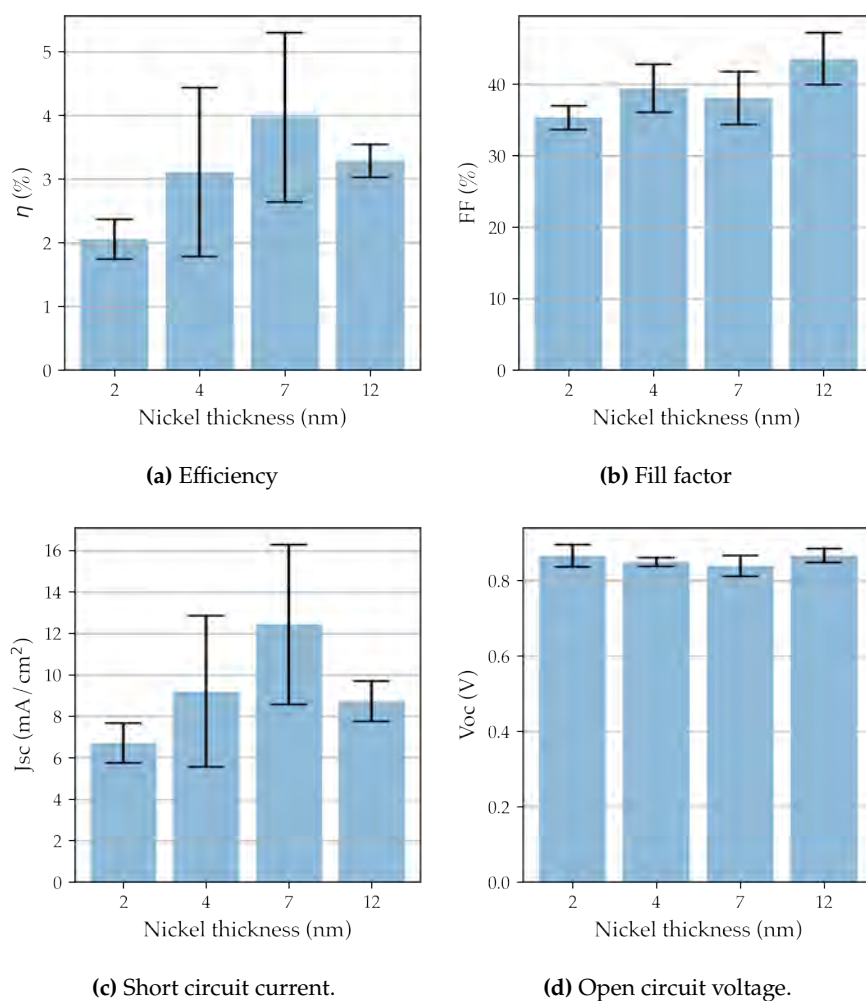


**Figure 4.2.:** A comparison of solar cell performance ( $\eta$ ,  $FF$ ,  $J_{SC}$  and  $V_{OC}$ ) for four different nickel thicknesses (2, 4, 7 and 12 nm)

Note that these measurements were made early in the optimization process, so the final reference cells reached significantly higher efficiencies, currents, fill factors, and voltages (see Figure 4.1).

## 4.2. Current-voltage measurements of the IBC cells

In this section the current-voltage measurements of the IBC devices as well as the contacting test to measure the system resistance are discussed.

### 4.2.1. IBC devices

Figure 4.3 shows the current-voltage curves of three types IBC cells, one with silver contacts and without perovskite (therefore not conducting), two with silver contacts and perovskite and two with silver contacts plus nickel oxide transport layers and perovskite.

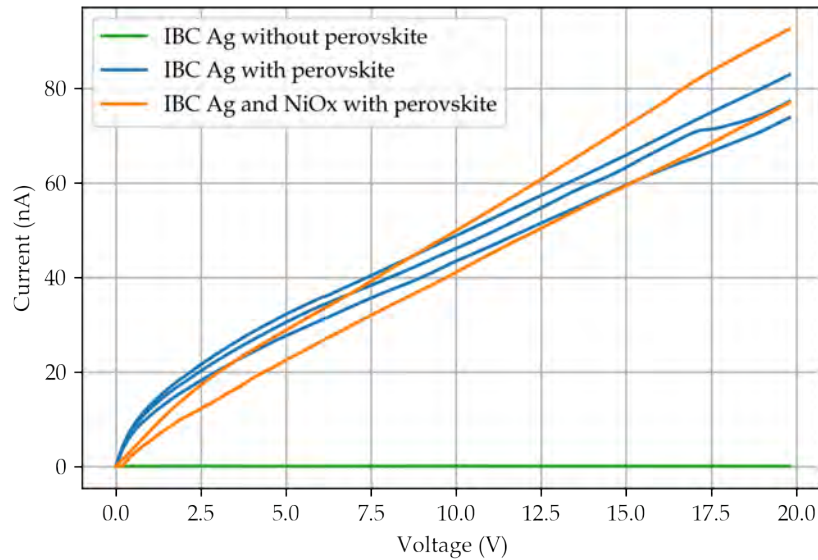
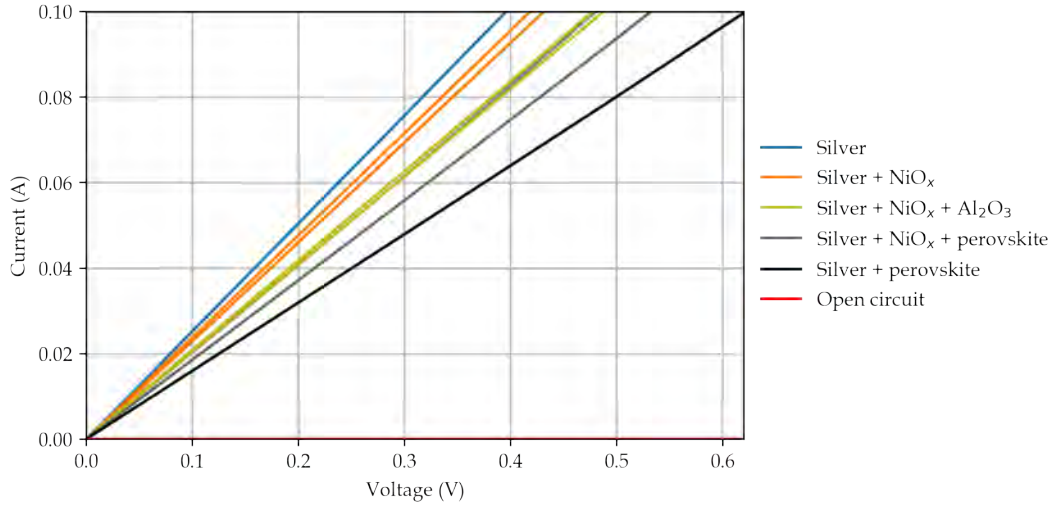


Figure 4.3.: Current-voltage curves of IBC devices.

The lines show that indeed the order of magnitude of the current of the IBC devices is much lower than for stacked cells. The expected low currents of an IBC device is explained in the theoretical background (section 2.6.1). One can also see the mostly linear IV-curve that we expected since it is not a p-i-n junction; the Ag device has no transport layers and the Ag + NiO<sub>x</sub> device has only hole transport layers.

### 4.2.2. Contacting test

As explained in paragraph 3.4.2 the limiting case for full coverage of the various layers is measured, to deduce the resistance of the measurement system. Figure 4.4 shows the results of measuring fully covered layers as a test of how well the IBC devices can be contacted with the probes (see Figure 3.15 for an image of this test). The plot shows that each layer adds extra resistance, but that the added layers still allow the sample to conduct in the same order of magnitude. The added resistance due to the extra layers is of a much lower order of magnitude than the resistance of an IBC cell (see the IV-curves in Figure 4.3), and therefore we conclude that the IBC cell can be well contacted using probes, despite the extra layers such as nickel oxide or perovskite.



**Figure 4.4.:** Current versus voltage for fully covered layers as a contacting test.

### 4.3. Drift-diffusion simulation

Figure 4.5 show the simulated electron and hole densities for varying bias. When comparing the two figures one can see that the hole density is ten orders of magnitude higher than the electron concentration. The simulated perovskite is set to be intrinsic rather than p-type. Therefore this higher hole concentration can be attributed to the presence of two HTL's and thereby holes diffusing out of the transport layers into the perovskite. Figure 4.5b shows that the hole density increases for increasing bias, due to the injected hole current.

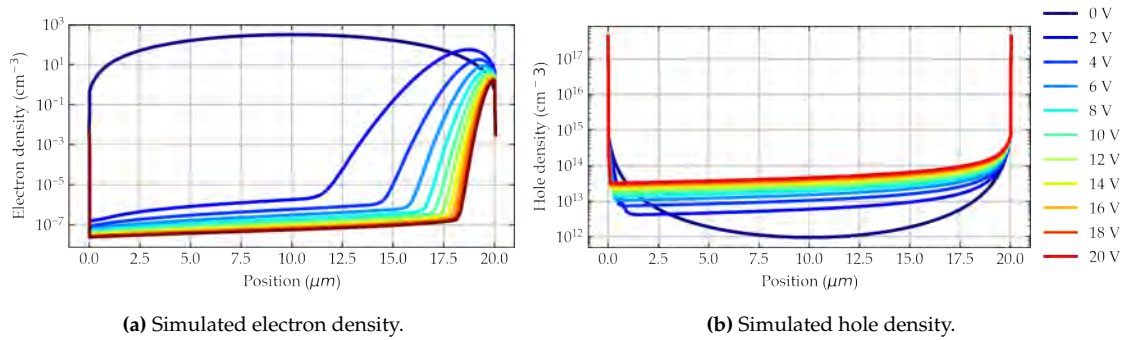


**Figure 4.5.:** Simulated charge densities for increasing bias.

Figures 4.5 a and b show the simulated band diagram of a hole-only device without bias and with a bias of 20 V. The band diagrams show that the band bends upwards towards both interfaces. This is related to the hole accumulation visible in the hole density plots.

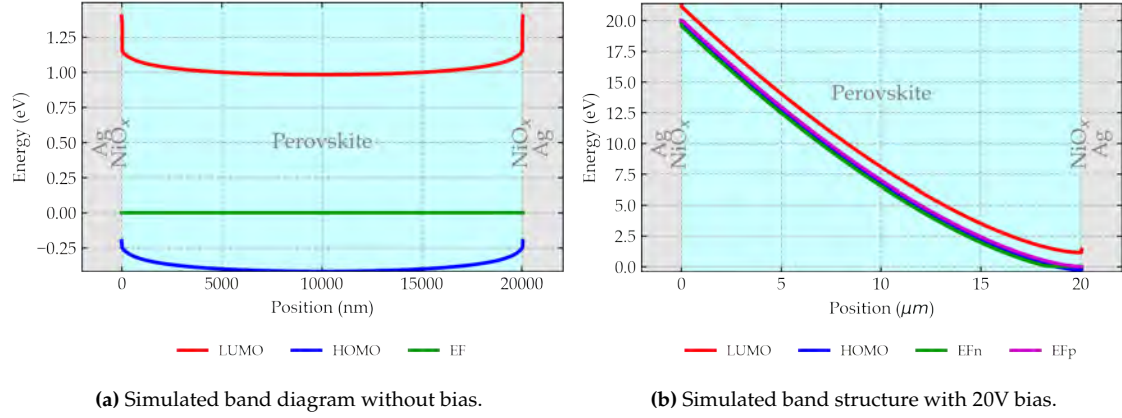


Figure 4.6.: Simulated band diagram with and without bias.

## 4.4. Spectrally and spatially resolved PL measurements under bias

### 4.4.1. PL spectra on and off contact

Figures 4.7 a and b show the PL spectrum above the contact and in between the contacts of the Ag device. Figure 4.7c indicates the position of these two spectra measurements. The Figure clearly shows that the PL above the contact is different from the PL in between the contacts. Above the contact, there is both a significantly lower PL as well as a peak shift. This shifted and decreased PL above the contact can be ascribed to the combination of two effects. First, Schötz et al. [50] showed that a peak shift or an apparent double peak can be caused by the presence of a reflective area underneath the perovskite. The photons emitted downwards can be reflected by the contact. This increases the total expected PL but also increases the distance the average emitted photon travels through the perovskite. Therefore a larger fraction of the photons is self-absorbed, causing a certain part of the spectrum of the PL to be quenched and leading to a redshift. Second, the overall decrease in PL above the contact, despite the reflective surface, can be ascribed to increased non-radiative recombination, as the absence of a transport layer allows charges to easily recombine in the silver contact.

As the shape of the spectrum above the contact is attributed to self-absorption it is a sum of an emission and absorbance spectrum, we fit the spectra with a sum of two Gaussians. The figure legends include the fitted parameters and this is the equation of a double Gaussian:

$$f(x) = A_1 \cdot \exp\left(-\frac{(x - \mu_1)^2}{2\sigma_1^2}\right) + A_2 \cdot \exp\left(-\frac{(x - \mu_2)^2}{2\sigma_2^2}\right) + B \quad (4.1)$$

Figure 4.7b shows the PL spectrum off and on the contact of the Ag + NiO<sub>x</sub> device. A similar effect is visible as at the Ag device; there is a peak shift, which can also be attributed to the increased self-absorption due to the reflective back, and there is a reduction in PL compared to the bulk. The reduction however is significantly less, which shows that the nickel oxide works effectively to block electrons. The fact that the PL off contact is still slightly lower compared to in between the contacts, despite the reflective back, is an indication that the interface indeed features loss mechanisms. As the band of nickel oxide aligns well with the perovskite and nickel oxide is known to be able to block electrons effectively [38], the most likely interface loss mechanism in this cases is trap-assisted recombination. However, other processes can also play a role in this reduced PL above the contact, such as the lower charge density above the contacts, as explained in paragraph 2.6.1 or the influence of the contact on the bulk morphology as explained in paragraph 2.5.



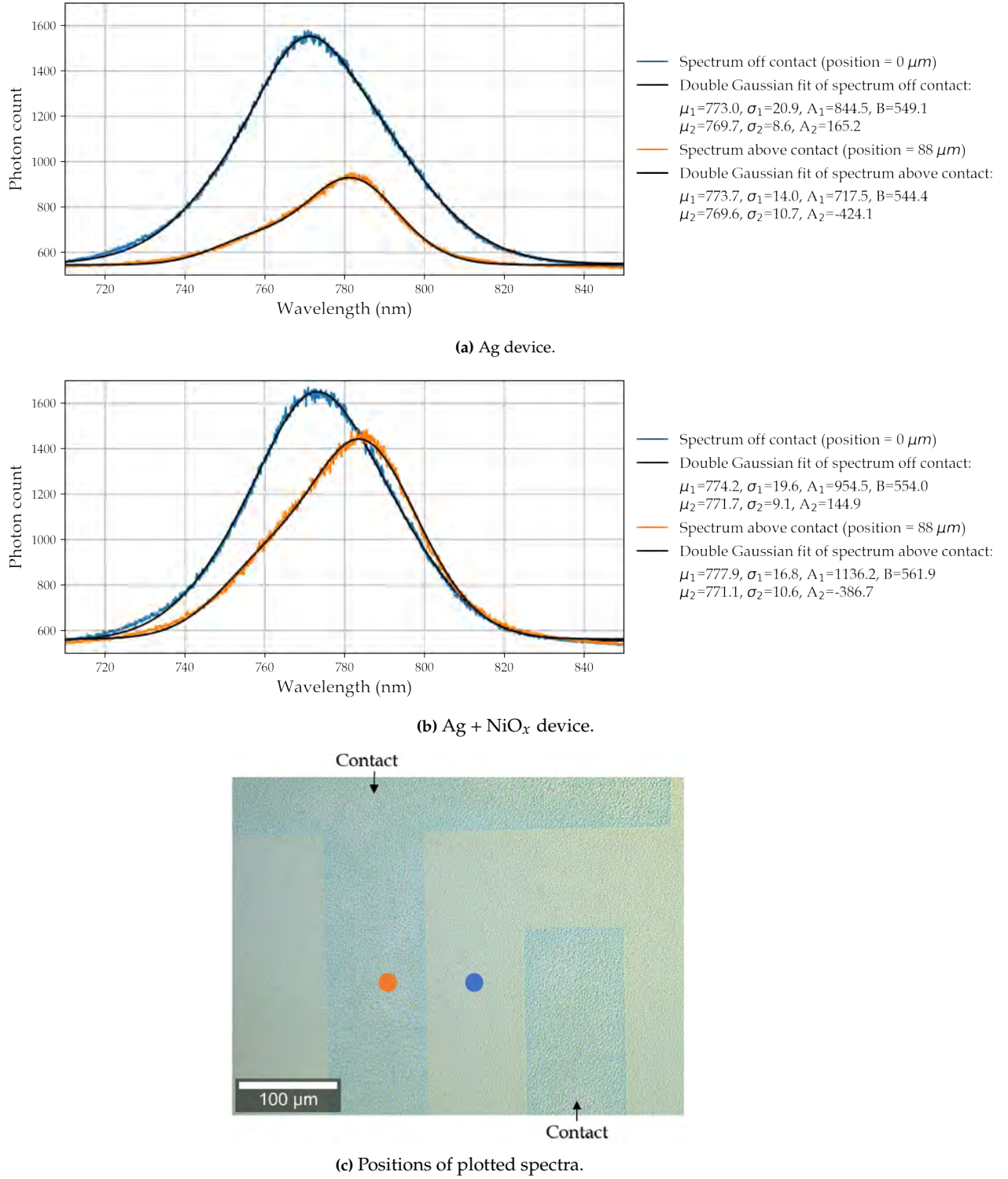
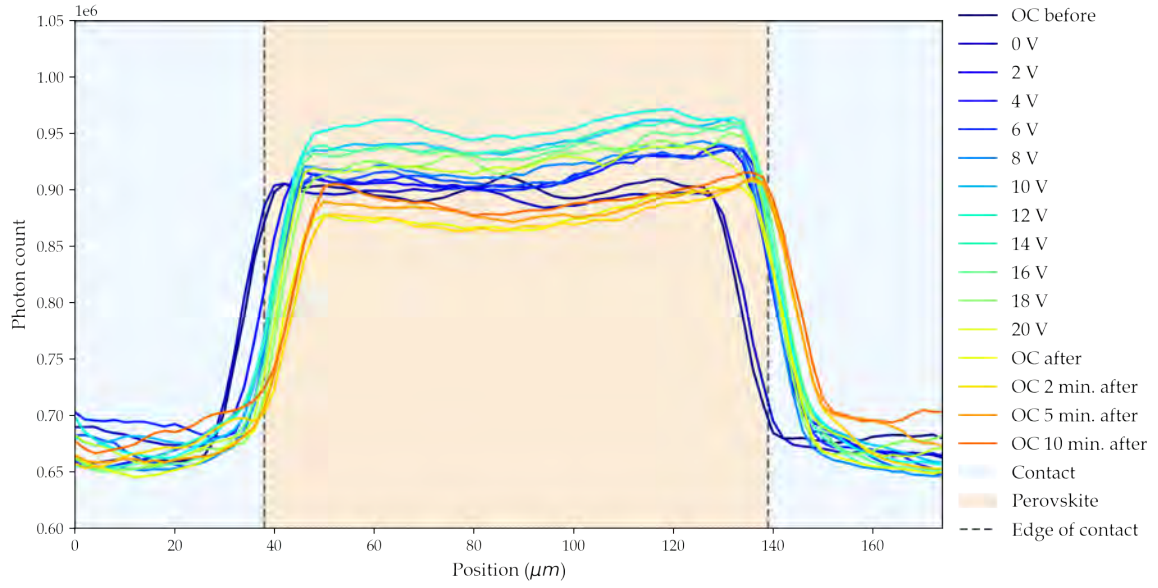


Figure 4.7.: Locations of plotted spectra; on contact (orange) off contact (blue).

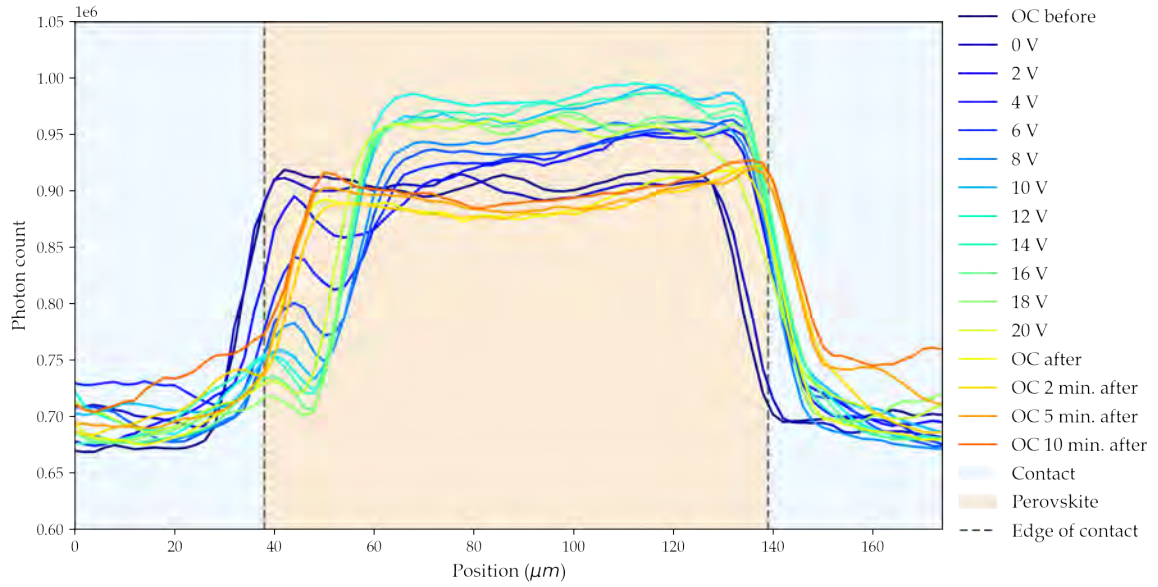
#### 4.4.2. Spatially resolved PL with varying bias of Ag device

Figure 4.8 a and b show the total photon count (summed over the whole spectrum from 710 to 850 nm) for each location, and a varying bias, ranging from 0 to 20 V in increments of 2 V, for the Ag device. In addition, the spatially resolved PL is shown without applying any bias, both before and after the biased measurements (denoting OC for open circuit). Each line scan has been executed twice (with a time

difference of 19.1 s), therefore Figure 4.8a shows the first line scan, and 4.8b shows the second line scan.



(a) First linescans of Ag device.



(b) Second linescans of Ag device.

**Figure 4.8.:** Ag device; total spatially resolved PL with 0 to 20 V bias.

The spatially and spectrally resolved PL of the Ag device shows different features above the contact, at the edges of the contacts, and in the bulk material. We discuss the characteristics of these three areas one by one.

#### Above the contact

Just as is visible in Figure 4.7a and discussed in section 4.4.1 there is both a redshift as well as a reduced PL above the contact, which can be described to a combination of self-absorption due to the reflective back and non-radiative recombination in the silver contact. Interestingly above the contact, there is no

clear relation between the voltage bias and the PL, with the various lines in mostly random order. The fact that the voltage has no clear influence above the middle of the contacts can be attributed to the fact that the path of least resistance for the current is through the edges of the contact rather than through the perovskite above the contact. Furthermore, we explained in paragraph 2.6.1 that most charges accumulate towards the edges. Therefore the injected current has less effect on the perovskite above the middle of the contact.

#### **In between the contacts (the bulk material)**

The PL in the bulk material shows a varying PL for the various lines. This can be attributed to two counteracting effects, the increasing charge concentration due to bias and degradation due to the laser. From 0 to 20 V an increase in PL as a function of the voltage is discernable. Our drift-diffusion model of a hole-only device predicted an increase in hole density for increasing voltage, due to the injected hole current (See Figure 4.5b). In this case, the Ag device can both conduct holes and electrons, so a higher density of both charges is expected with increasing current. Richter et al. [51] showed that increased charge concentration leads to an increased rate in the change of the charge concentration, which in this case translates to an increased PL. Therefore, the increasing PL with increasing voltage in the bulk material can be ascribed to the higher charge density when a bias is applied. The uncontacted (open circuit) lines after the biased measurements show a decrease in PL, relative to the uncontacted lines before the biased measurement. This can be attributed to decay processes caused by the combination of the current and laser. Interestingly, the PL appears to partly recover from this degradation after five to ten minutes.

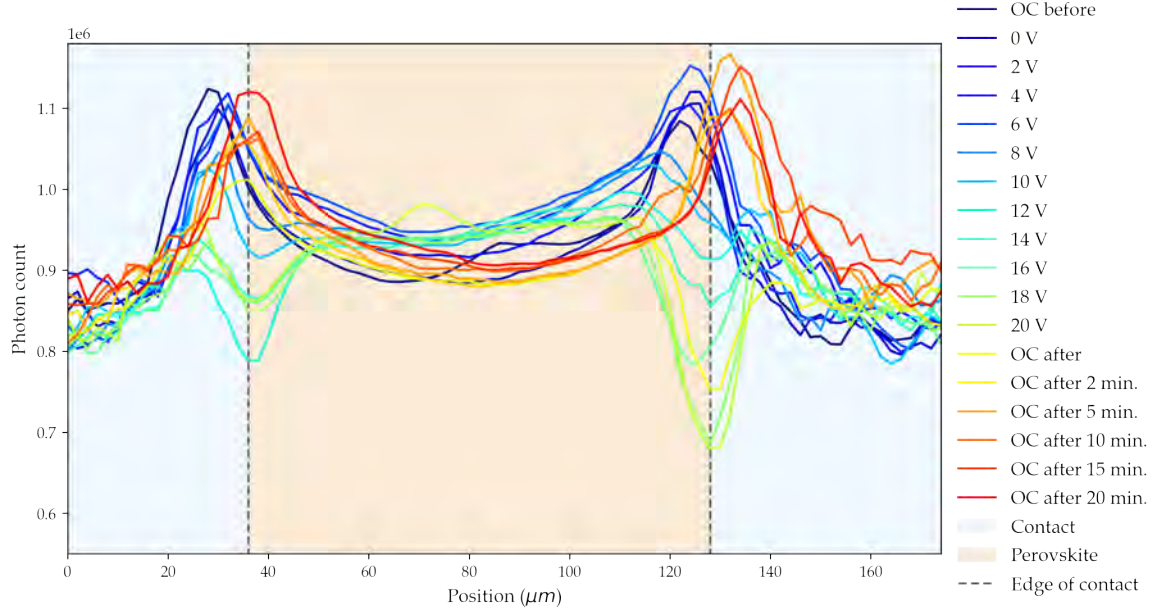
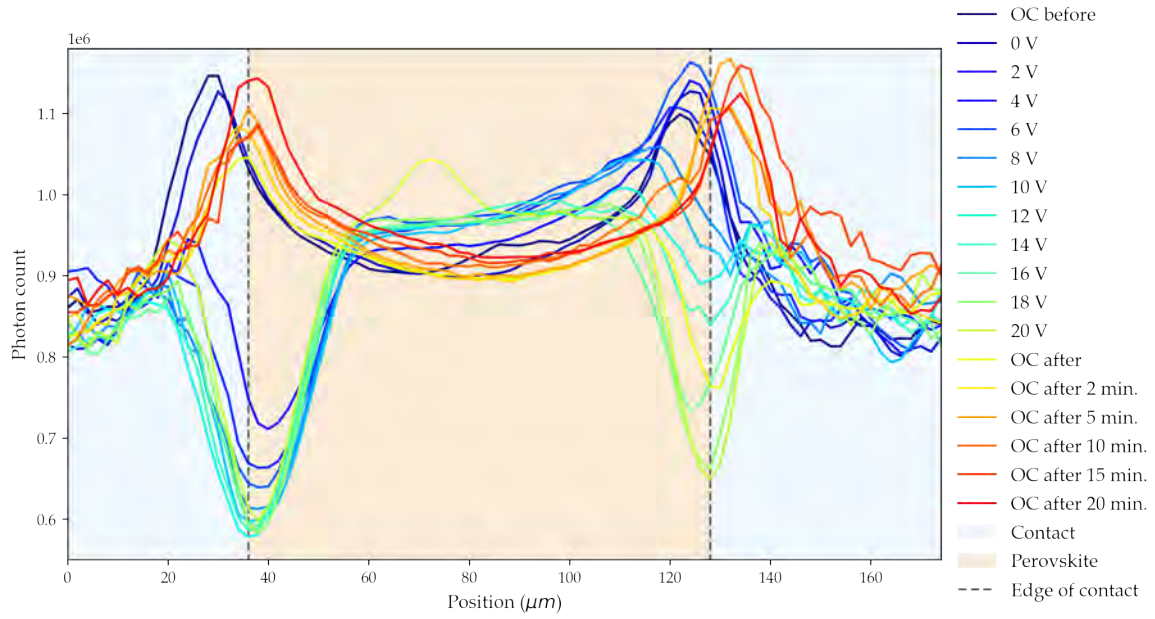
#### **Above the edges of the contacts**

At the edges of the contacts, three effects can be distinguished. First of all, the shape of the graph appears to shift from left to right. This, however, is not an effect of the voltage but is purely caused by geometry. The sample was not perfectly aligned with the x-y stage, therefore each time the sample was moved several  $\mu\text{m}$ 's to measure a line scan at a new location, the position of the edge was also slightly moved (see Figure 3.17). Second, an interesting feature is visible when comparing the first and second line scans (figures 4.8 a and b). In the second line scan, there is significant quenching of the PL around the edge of the positive (left) contact. As this effect happens only after the first line scan (19.1 seconds later) it can not be solely an electric effect, which would happen at a much faster time scale. It, therefore, is likely related to the migration of ions, either from the perovskite into the silver or the other way around, induced by the combination of the probing laser and the voltage. The direction of the electric field from the biased contacts would move a positive Ag particle away from the contact or a negative ion towards the contact. A possible likely candidate would be the movement of silver ions towards the perovskite, or iodide ions towards the contact. Third, there is a small bump visible within the quenched range of the left interface. This small bump could be a sign of an injection barrier at the interface, leading to a localized accumulation of charges at the interface.

#### **4.4.3. Spatially resolved PL with a varying bias of Ag + NiO<sub>x</sub> device**

Having unpacked the various effects for the PL of the Ag device, we now move on to the Ag + NiO<sub>x</sub> device. Just as with the Ag device, each line scan was executed twice. The Appendix also includes a Figure of a measurement taken minutes after this, but with reversed bias see Figure A.2. Just as with the silver device, various effects can be distinguished at three different regions; above the contacts, in the bulk material (in between the contacts), and around the edges of the contacts. Let us discuss the effects and their likely causes at each region, beginning with the contacts.



(a) First linescans of Ag + NiO<sub>x</sub> device.(b) Second linescans of Ag + NiO<sub>x</sub> device.**Figure 4.9.:** Total photon count for spatially resolved PL with 0 to 20 V.

### Above the contacts

Above the contacts, we see the same features we discussed in section 4.4.1. A redshift is visible which can be attributed to the increased self-absorption due to the reflective back, and there is a reduction in PL compared to the bulk as discussed and attributed in section 4.4.1. Just as was the case for the Ag device, in the middle of the contact there is no clear relation between the PL and the voltage bias, which can be attributed to the fact that most current will not be flowing above the contact, and to the fact that most charges do not accumulate in the middle but towards the edges of the contacts.

### In the bulk material (in between the contacts)

In the middle, the lines show the PL in between the contacts. Two remarks can be made concerning the bulk PL of the Ag + NiO<sub>x</sub> device. First, the lines show an increasing PL with increasing bias voltage. Just as is the case with the Ag device, this can be explained by the increased charge concentration, due to the injected hole current. Second, where the Ag device shows some decrease in PL ascribed to degradation, this sample does not have a lower PL after the measurement. This suggests that the HTL layer prevents the degradation process in the bulk material that the Ag device is subject to. A possible explanation is that the NiO<sub>x</sub> layers block Ag<sup>+</sup> ions to migrate into the perovskite.

### Above the edge of the contacts

Two remarkable effects are visible above the edge of the contacts of the Ag + NiO<sub>x</sub> device. The PL around the edge in a region of  $\pm 15 \mu\text{m}$  is significantly increased. This increase could be explained by two different hypotheses. Both hypotheses are related to the fact that the hole density simulated by the drift-diffusion model without bias, shows hole accumulation at the interface due to hole diffusion from the p-type nickel oxide layer. Combined with the charge distribution of a conductive strip (as explained in section 2.6.1, this means that most charge accumulation towards the interface happens around the edge of contact. These increased hole concentrations around the edges of the contacts could lead to the measured increased PL in two different ways. This higher concentration of holes could be an explanation of an increased PL around the edge of the contact as electrons can more easily radiatively recombine. Another possible explanation for this increased PL above the edge of the contacts when unbiased could be the filling of vacancies. If the perovskite has significant vacancies, the area around the edge could benefit from negative ions (iodide or bromide) migrating from other parts of the perovskite due to the electric field caused by the increased hole concentration.

A second important feature of the PL above the edges is the remarkable decrease in PL once the contacts are biased. As visible in the color scale plot (Figure A.4d in the Appendix) at its lowest point, the PL above the edges is reduced to close to the background level. In other words, whereas the PL at the edges is increased without a bias, it is almost completely quenched with a bias. The lines also show that this quenching is increased for higher voltage and happens at both contacts. When comparing Figures 4.9 a and b, one can see that this quenching (especially at the positive contact edge) happens gradually and is further increased during the second line scan (37.4 seconds later). Just as was the case with the Ag device's PL quenching at the edge of the contact, this means that this effect cannot solely be an electric effect, and is likely caused by ion migration. So this means that the combination of the probing laser, as well as the bias voltage and the electric field of the hole accumulation around the edges of the contacts all together, causes ions to migrate from around the edge of the contact.

# Conclusions & Outlook 5.

To analyze the processes present at the interface between the perovskite and nickel oxide HTL, we measure the spectrally and spatially resolved PL of hole-only IBC devices. First, for reference and optimization, we fabricate stacked cells, run a drift-diffusion model, execute a contacting test, and measure the current-voltage characteristics of hole-only IBC devices. The current-voltage curves of the stacked reference solar cells show that e-beam evaporated nickel that is then oxidized to nickel oxide at 450 °C for 20 minutes can work as an effective HTL, with a best-cell PCE of 9.76%. Furthermore, we find an optimal thickness of evaporated nickel layer at 7 nm. The drift-diffusion model of a hole-only nickel oxide device with a 20  $\mu\text{m}$  perovskite layer shows significant hole accumulation towards the nickel oxide interface with associated upwards band bending towards the interface. A contacting test shows that the extra layers of nickel oxide and perovskite did not inhibit the contacting of the IBC device using electric probes.

The spatially and spectrally resolved PL measurements of the hole-only device can distinguish several localized processes within the device. Increased self-absorbance above the contact due to the reflectivity of the contact is visible as a redshift in PL. Interface recombination and lower charge concentration are visible as a decrease in PL above the contact. In between the contacts an increasing hole concentration due to the injected hole current is visible as an increase in PL. An indication of an injection barrier is visible as a small bump in PL at the edge of the contact.

Two main conclusions can be drawn concerning what is happening at the interface. First, both our drift-diffusion model as well as the PL measurements indicate that the interface of nickel oxide and perovskite features significant hole accumulation with associated band bending. This is visible in the PL measurements as an increased PL at the edges of the contacts. Second, we conclude that ion migration plays an important role in the processes at the interface. This can be seen from the fact that the voltage-induced reduction in PL at the edge of the contact changes over the long timescale of tens of seconds.

The architecture of the IBC device combined with a voltage bias makes it possible to disentangle and localize the above-mentioned processes. This research, therefore, shows the potential of this setup to further analyze and localize the mechanisms present at the interface and in the bulk material.

To verify and expand understanding of these processes and conclusions it would be worthwhile to carry out further experiments, such as creating a two-dimensional drift-diffusion model, measuring the temporally resolved PL, analyzing passivation layers, and fabricating asymmetric IBC cells. A two-dimensional drift-diffusion model, that incorporates the IBC structure and can be illuminated and probed locally, would be able to simulate the two-dimensional dynamics of an IBC device and would make it possible to compare the model with the measurements more directly (similar to what was done by Prince et al. [52]). Measuring the temporally resolved PL (time-controlled single photon counting) would allow to further disentangle the mechanisms at the interface. It would be worthwhile to fabricate an IBC device with an extra passivation layer on top of the nickel oxide HTL, that is shown to improve its efficiency, such as a 2D perovskite layer or a self-assembled monolayer [53]. Comparing the spatially resolved PL of devices with and without these layers could shine a light on the causes behind its improved efficiency. Using an asymmetric IBC cell, with both an HTL and an ETL would make it possible to benefit from the extra insights of a spatially resolved PL, with a complete cell as well. Such an asymmetric IBC cell would feature the processes of charge separation and extraction and could thereby enrich the added insights of a spatially resolved PL measurement.



# Bibliography

Here are the references in citation order.

- [1] Raj Kumar. *Atomic Molecular Spectra: Laser*. KNRN, 2012 (cited on page 3).
- [2] Z Zhu et al. 'AR6 Climate Change 2021: The Physical Science Basis'. In: *IPCC: Geneva, Switzerland* (2021) (cited on page 3).
- [3] Conference of the Parties. 'Paris agreement'. In: *Report of the Conference of the Parties to the United Nations Framework Convention on Climate Change (21st Session, 2015: Paris)*. Retrived December. Vol. 4. HeinOnline. 2015, p. 2017 (cited on page 3).
- [4] Dolf Gielen et al. 'World Energy Transitions Outlook: 1.5° C Pathway'. In: (2021) (cited on page 3).
- [5] Martin Green et al. 'Solar cell efficiency tables (version 57)'. In: *Progress in photovoltaics: research and applications* 29.1 (2021), pp. 3–15 (cited on pages 3, 11).
- [6] Bo Chen et al. 'Imperfections and their passivation in halide perovskite solar cells'. In: *Chemical Society Reviews* 48.14 (2019), pp. 3842–3867 (cited on pages 3, 11).
- [7] Minmin Yang et al. 'Hotspots, frontiers, and emerging trends of tandem solar cell research: A comprehensive review'. In: *International Journal of Energy Research* (2022) (cited on page 3).
- [8] William Shockley and Hans J Queisser. 'Detailed balance limit of efficiency of p-n junction solar cells'. In: *Journal of applied physics* 32.3 (1961), pp. 510–519 (cited on pages 3, 9).
- [9] Benjia Dou et al. 'Roll-to-roll printing of perovskite solar cells'. In: *ACS Energy Letters* 3.10 (2018), pp. 2558–2565 (cited on pages 3, 11).
- [10] Maithili K Rao et al. 'Review on persistent challenges of perovskite solar cells' stability'. In: *Solar Energy* 218 (2021), pp. 469–491 (cited on pages 3, 11).
- [11] Weijun Ke and Mercouri G Kanatzidis. 'Prospects for low-toxicity lead-free perovskite solar cells'. In: *Nature communications* 10.1 (2019), pp. 1–4 (cited on page 3).
- [12] Lingfeng Chao et al. 'Solvent Engineering of the Precursor Solution toward Large-Area Production of Perovskite Solar Cells'. In: *Advanced Materials* 33.14 (2021), p. 2005410 (cited on page 3).
- [13] Katelyn P Goetz et al. 'Shining light on the photoluminescence properties of metal halide perovskites'. In: *Advanced Functional Materials* 30.23 (2020), p. 1910004 (cited on pages 4, 16).
- [14] Michael Grätzel. 'The rise of highly efficient and stable perovskite solar cells'. In: *Accounts of chemical research* 50.3 (2017), pp. 487–491 (cited on page 4).
- [15] Martin Green, Anita Ho-Baillie, and Henry J Snaith. 'The emergence of perovskite solar cells'. In: *Nature photonics* 8.7 (2014), pp. 506–514 (cited on pages 7, 10).
- [16] Bruno Ehrler et al. *Photovoltaics reaching for the Shockley–Queisser limit*. 2020 (cited on pages 9, 10).

- [17] Akihiro Kojima et al. 'Novel photoelectrochemical cell with mesoscopic electrodes sensitized by lead-halide compounds (2)'. In: *ECS Meeting Abstracts*. 7. IOP Publishing. 2006, p. 397 (cited on page 10).
- [18] Qingfeng Dong et al. 'Electron-hole diffusion lengths > 175  $\mu\text{m}$  in solution-grown  $\text{CH}_3\text{NH}_3\text{PbI}_3$  single crystals'. In: *Science* 347.6225 (2015), pp. 967–970 (cited on page 11).
- [19] Luis M Pazos-Outón et al. 'Photon recycling in lead iodide perovskite solar cells'. In: *Science* 351.6280 (2016), pp. 1430–1433 (cited on page 11).
- [20] Sayak Bhattacharya and Sajeew John. 'Beyond 30% conversion efficiency in silicon solar cells: a numerical demonstration'. In: *Scientific reports* 9.1 (2019), pp. 1–15 (cited on page 11).
- [21] Tianhao Wu et al. 'The main progress of perovskite solar cells in 2020–2021'. In: *Nano-Micro Letters* 13.1 (2021), pp. 1–18 (cited on page 11).
- [22] Narasak Pandech et al. 'Effects of the van der Waals Interactions on Structural and Electronic Properties of  $\text{CH}_3\text{NH}_3(\text{Pb}, \text{Sn})(\text{I}, \text{Br}, \text{Cl})_3$  Halide Perovskites'. In: *ACS omega* 5.40 (2020), pp. 25723–25732 (cited on page 11).
- [23] Long Ji et al. 'Regulating crystallization dynamics and crystal orientation of methylammonium tin iodide enables high-efficiency lead-free perovskite solar cells'. In: *Nanoscale* (2022) (cited on page 11).
- [24] Giorgio Schileo and Giulia Grancini. 'Lead or no lead? Availability, toxicity, sustainability and environmental impact of lead-free perovskite solar cells'. In: *Journal of Materials Chemistry C* 9.1 (2021), pp. 67–76 (cited on page 11).
- [25] Eline M Hutter et al. 'Metal halide perovskite toxicity effects on plants are caused by iodide ions'. In: *arXiv preprint arXiv:2012.06219* (2020) (cited on page 11).
- [26] Nam-Gyu Park. 'Green solvent for perovskite solar cell production'. In: *Nature Sustainability* 4.3 (2021), pp. 192–193 (cited on page 11).
- [27] Wenjing Yu et al. 'Recent advances on interface engineering of perovskite solar cells'. In: *Nano Research* 15.1 (2022), pp. 85–103 (cited on page 11).
- [28] Tejas S Sherkar et al. 'Recombination in perovskite solar cells: significance of grain boundaries, interface traps, and defect ions'. In: *ACS energy letters* 2.5 (2017), pp. 1214–1222 (cited on page 11).
- [29] Weidong Zhu et al. 'Band Alignment Engineering Towards High Efficiency Carbon-Based Inorganic Planar  $\text{CsPbI}_2\text{Br}$  Perovskite Solar Cells'. In: *ChemSusChem* 12.10 (2019), pp. 2318–2325 (cited on page 12).
- [30] Iván Mora-Seró. 'How do perovskite solar cells work?' In: *Joule* 2.4 (2018), pp. 585–587 (cited on page 12).
- [31] Jin-Wook Lee et al. 'Verification and mitigation of ion migration in perovskite solar cells'. In: *APL materials* 7.4 (2019), p. 041111 (cited on page 12).
- [32] Teng Zhang, Chen Hu, and Shihe Yang. 'Ion Migration: A "Double-Edged Sword" for Halide-Perovskite-Based Electronic Devices'. In: *Small Methods* 4.5 (2020), p. 1900552 (cited on page 12).



- [33] Guang Yang et al. 'Interface engineering in planar perovskite solar cells: energy level alignment, perovskite morphology control and high performance achievement'. In: *Journal of Materials Chemistry A* 5.4 (2017), pp. 1658–1666 (cited on page 12).
- [34] Kunta Yoshikawa et al. 'Silicon heterojunction solar cell with interdigitated back contacts for a photoconversion efficiency over 26%'. In: *Nature energy* 2.5 (2017), pp. 1–8 (cited on page 13).
- [35] Weichuang Yang et al. 'Optical design and optimization for back-contact perovskite solar cells'. In: *Solar Energy* 201 (2020), pp. 84–91 (cited on page 13).
- [36] Gerald L Pollack and Daniel R Stump. *Conducting Strip by Conjugate Functions, Electromagnetism*. American Association of Physics Teachers, 2005. Section 5.4. Retrieved from: <https://web.pa.msu.edu/people/stump/EM/chap5/5ex2.pdf> (cited on page 13).
- [37] J Zhang et al. 'A simple and dopant-free hole-transporting material based on (2-ethylhexyl)-9 H-carbazole for efficient planar perovskite solar cells'. In: *Journal of Materials Chemistry C* 5.48 (2017), pp. 12752–12757 (cited on page 15).
- [38] Xingtian Yin et al. 'Nickel oxide as efficient hole transport materials for perovskite solar cells'. In: *Solar RRL* 3.5 (2019), p. 1900001 (cited on pages 15, 16, 35).
- [39] T Selvan Ponmudi et al. 'Comparative study on the effect of annealing temperature on sol-gel-derived nickel oxide thin film as hole transport layers for inverted perovskite solar cells'. In: *Journal of Materials Science: Materials in Electronics* 32.6 (2021), pp. 8157–8166 (cited on page 15).
- [40] Dibyashree Koushik et al. 'Plasma-assisted atomic layer deposition of nickel oxide as hole transport layer for hybrid perovskite solar cells'. In: *Journal of Materials Chemistry C* 7.40 (2019), pp. 12532–12543 (cited on page 15).
- [41] Zonghao Liu et al. 'Nickel oxide nanoparticles for efficient hole transport in pin and nip perovskite solar cells'. In: *Journal of Materials Chemistry A* 5.14 (2017), pp. 6597–6605 (cited on page 16).
- [42] Ziye Liu et al. 'High-Performance Planar Perovskite Solar Cells Using Low Temperature, Solution-Combustion-Based Nickel Oxide Hole Transporting Layer with Efficiency Exceeding 20%'. In: *Advanced Energy Materials* 8.19 (2018), p. 1703432 (cited on page 16).
- [43] Diego Di Girolamo et al. 'Anodically electrodeposited NiO nanoflakes as hole selective contact in efficient air processed pin perovskite solar cells'. In: *Solar Energy Materials and Solar Cells* 205 (2020), p. 110288 (cited on page 16).
- [44] Guijun Li et al. 'Overcoming the limitations of sputtered nickel oxide for high-efficiency and large-area perovskite solar cells'. In: *Advanced Science* 4.12 (2017), p. 1700463 (cited on page 16).
- [45] Jong Hoon Park et al. 'Efficient CH<sub>3</sub>NH<sub>3</sub>PbI<sub>3</sub> perovskite solar cells employing nanostructured p-type NiO electrode formed by a pulsed laser deposition'. In: *Advanced Materials* 27.27 (2015), pp. 4013–4019 (cited on page 16).
- [46] Menglei Feng et al. 'High-Efficiency and Stable Inverted Planar Perovskite Solar Cells with Pulsed Laser Deposited Cu-Doped NiO x Hole-Transport Layers'. In: *ACS Applied Materials & Interfaces* 12.45 (2020), pp. 50684–50691 (cited on page 16).
- [47] Tobias Abzieher et al. 'Electron-beam-evaporated nickel oxide hole transport layers for perovskite-based photovoltaics'. In: *Advanced Energy Materials* 9.12 (2019), p. 1802995 (cited on page 16).

- [48] Martin Stolterfoht et al. 'Voltage-dependent photoluminescence and how it correlates with the fill factor and open-circuit voltage in perovskite solar cells'. In: *ACS Energy Letters* 4.12 (2019), pp. 2887–2892 (cited on pages 16, 17).
- [49] Rabih Zaouk, Benjamin Park, and Marc Madou. 'Introduction to Microfabrication Techniques'. In: *Methods in molecular biology (Clifton, N.J.)* 321 (Feb. 2006), pp. 5–15. doi: [10.1385/1-59259-997-4:3](https://doi.org/10.1385/1-59259-997-4:3) (cited on page 21).
- [50] Konstantin Schötz et al. 'Double peak emission in lead halide perovskites by self-absorption'. In: *Journal of Materials Chemistry C* 8.7 (2020), pp. 2289–2300 (cited on page 35).
- [51] Johannes M Richter et al. 'Enhancing photoluminescence yields in lead halide perovskites by photon recycling and light out-coupling'. In: *Nature communications* 7.1 (2016), pp. 1–8 (cited on page 38).
- [52] Kevin J Prince et al. 'Complementary interface formation toward high-efficiency all-back-contact perovskite solar cells'. In: *Cell Reports Physical Science* 2.3 (2021), p. 100363 (cited on page 41).
- [53] Nga Phung et al. 'Enhanced Self-Assembled Monolayer Surface Coverage by ALD NiO in pin Perovskite Solar Cells'. In: *ACS Applied Materials & Interfaces* (2021) (cited on page 41).



In this Appendix we show various results that were not included in the results section, such as color scale visualisation of the spatially and spectrally resolved bias, plots of the fitted peak positions, a similar measurement as Figure 4.9 but with reversed bias and a  $C_{60}$  lift off test. These plots show among others the rich data sets that biased spatially resolved PL measurements of IBC devices yield.

## A.1. Current during the spatially resolved PL measurements.

Figure A.1 shows the current during the spatially resolved PL measurements for both the Ag and Ag+ $NiO_x$  devices.

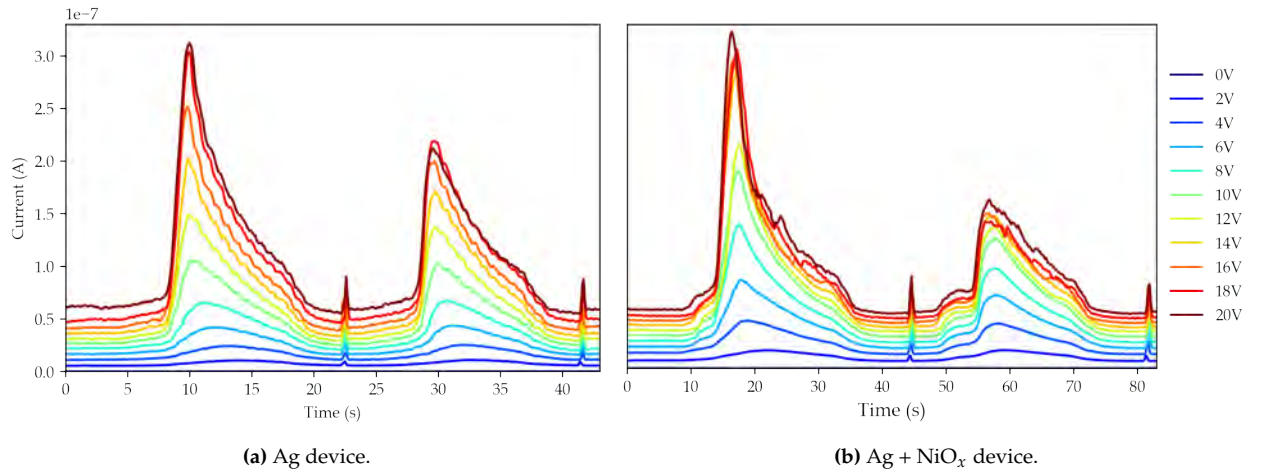
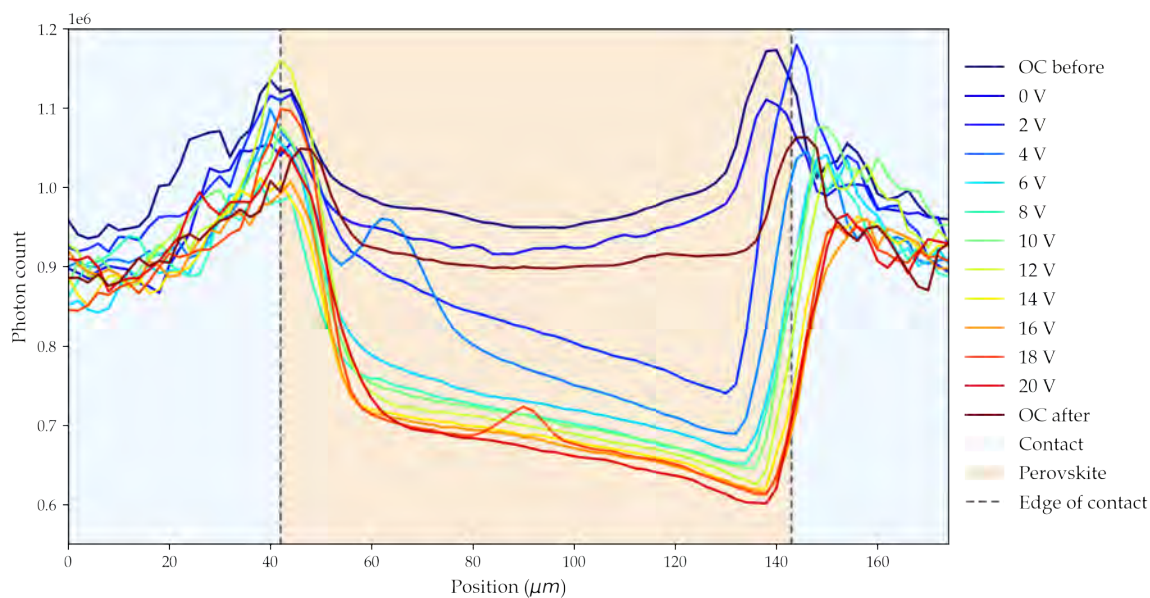


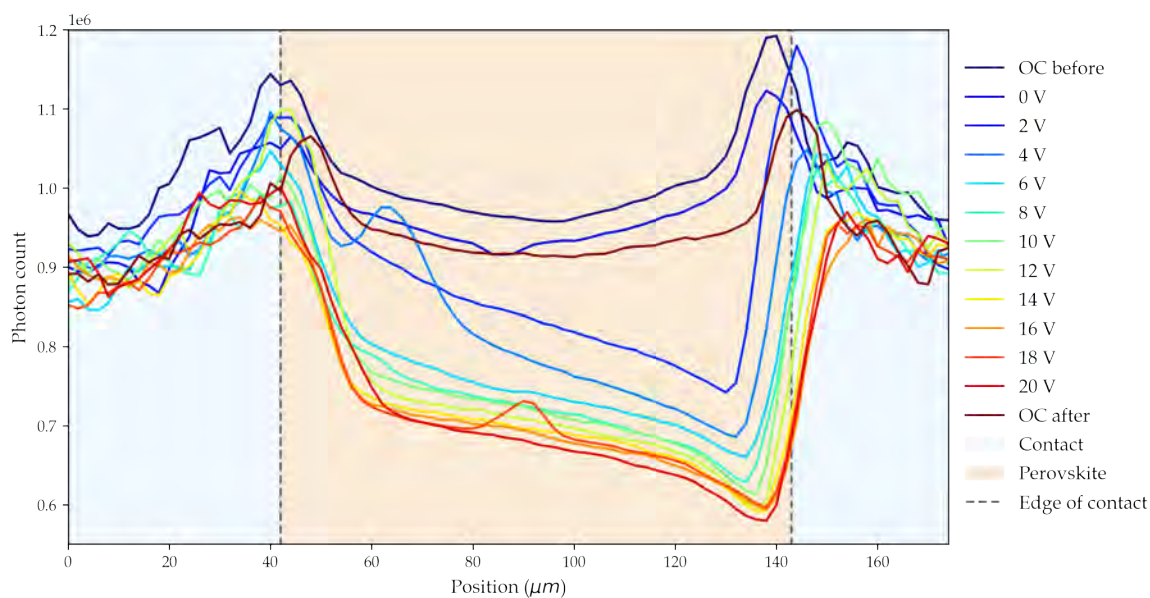
**Figure A.1.:** Current during linescan for all biases.

## A.2. Reversed bias measurement

Right after the measurements of Figure 4.9 we execute the same measurement but with reversed bias. Figure A.2 shows this reversed bias spatially resolved PL measurement.



(a) First linescans of Ag + NiO<sub>x</sub> device.



(b) Second linescans of Ag + NiO<sub>x</sub> device.

**Figure A.2.:** Total photon count for spatially resolved PL with 0 to 20 V, several minutes after the measurement of Figure 4.9 but with reversed bias.

### A.3. Position of fitted peaks of spectra

Figure A.3 shows the peaks of the fitted spectra for each location and for each bias of both the Ag and Ag + NiO<sub>x</sub> device.

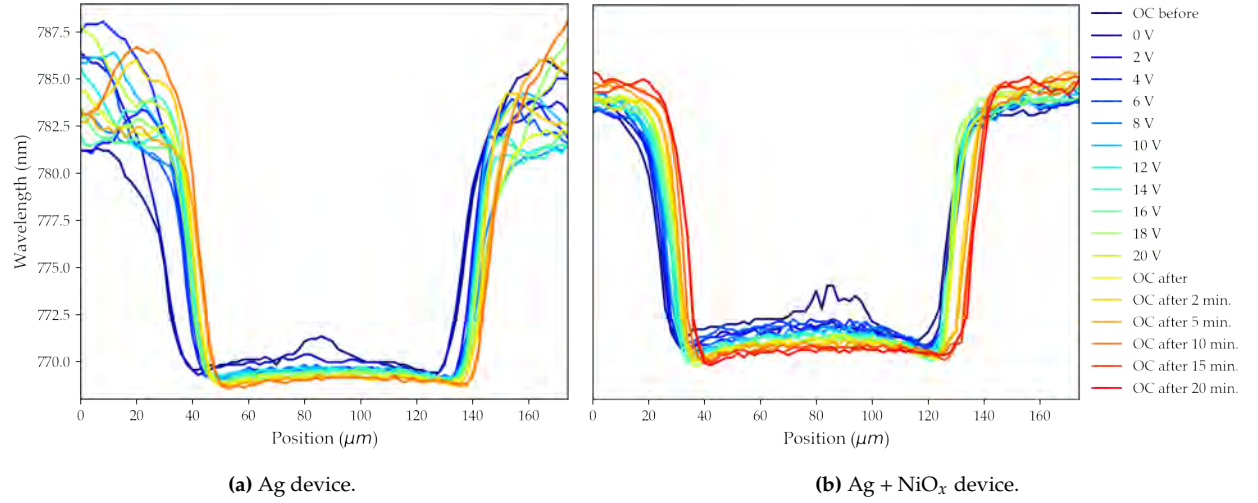


**Figure A.3.:** Position of peak of fitted spectrum for all biases.

## A.4. Color scale visualization of spatially and spectrally resolved spectra

Figure A.4 shows the spectra at each location for the Ag and Ag + NiO<sub>x</sub> device in a color scale visualization. The x-axis shows the location, the y-axis the wavelength and the color shows the photon count. In these figures, the spectra of the biased cells (18 V) are included as well. The peak positions are determined with the same double Gaussian fit as explained in section 4.4.1. Figure A.4d shows that the reduction in PL above the edge of the contact when biased, is as low as the background PL at the ends of the spectrum.

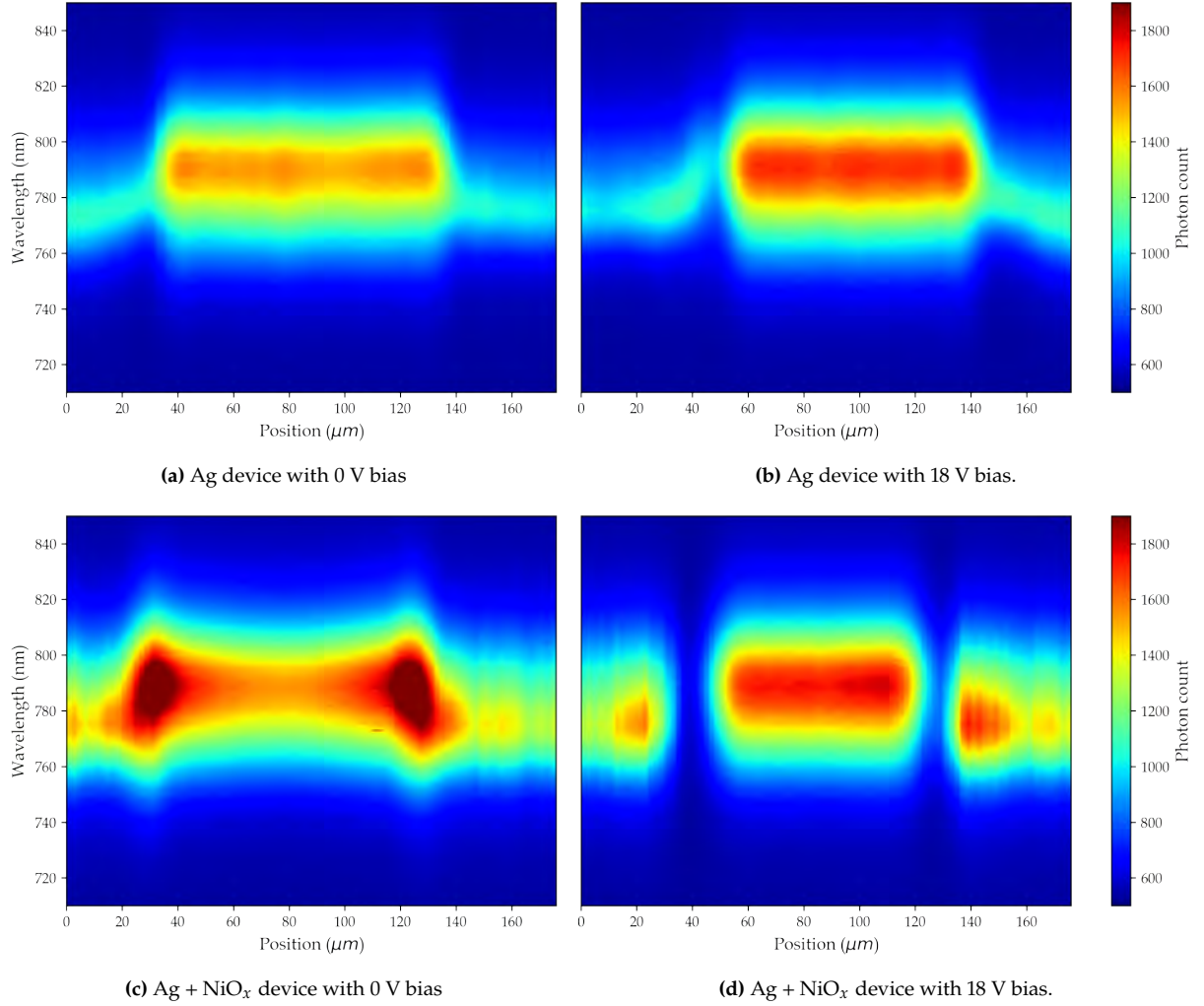


**Figure A.4.:** PL Spectra for each location for the Ag and Ag + NiO<sub>x</sub> device with a bias of 0 and 20 V (all showing the second linescans).

## A.5. $C_{60}$ lift off test

In order to explore the possibility of using buckminsterfullerene ( $C_{60}$ ) as the ETL for the IBC devices we have tested the extent to which  $C_{60}$  can withstand the lift-off and spincoating procedure. Figure ?? shows the absorbance of an ITO sample (blue), the same ITO sample with 30 nm evaporated  $C_{60}$  (orange), and before and after liftoff or spincoating procedure (green). As the absorbance of the sample returns to the original ITO's absorbance, we conclude that the  $C_{60}$  is completely removed both by the liftoff procedure as well as the spincoating procedure. For this reason  $C_{60}$  is not a suitable ETL for our design of IBC devices.

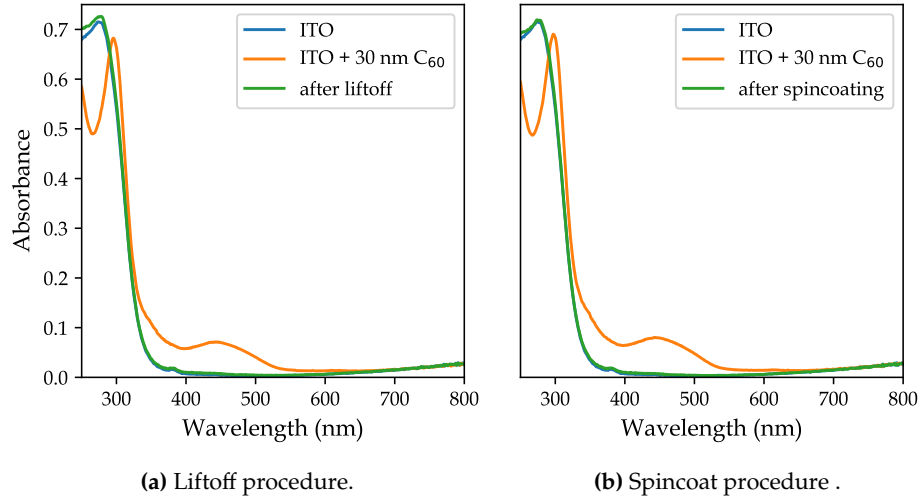


**Figure A.5.:** Absorbance of ITO sample with and with 30 nm  $C_{60}$ , before and after liftoff or spincoat procedure.